

Original Article


Cite this article: Ou Q, Lai J-Q, Carvalho BB, Zi F, Jiang Z-Q, Wang K, and Liu Y-Z (2021) Early Silurian granitic rocks and associated enclaves as evidence of rapid cooling in a cognate magma system: the case of the Xuehuading–Panshanchong pluton, South China Block. *Geological Magazine* **158**: 1173–1193. <https://doi.org/10.1017/S0016756820001144>

Received: 13 April 2020
Revised: 4 September 2020
Accepted: 22 September 2020
First published online: 19 November 2020

Keywords:
enclaves; early Silurian granitic rocks;
heterogeneous source; disequilibrium melting;
South China Block

Authors for correspondence:
Quan Ou, Email: ouquanCSU@126.com;
Jian-Qing Lai, Email address:ljq@csu.edu.cn

Early Silurian granitic rocks and associated enclaves as evidence of rapid cooling in a cognate magma system: the case of the Xuehuading–Panshanchong pluton, South China Block

Quan Ou^{1,2} , Jian-Qing Lai², Bruna B. Carvalho³, Feng Zi⁴, Zi-Qi Jiang⁵, Kun Wang⁶ and Yi-Zhi Liu⁵

¹State Key Laboratory of Oil and Gas Reservoir Geology and Exploitation, Institute of Sedimentary Geology, Chengdu University of Technology, Chengdu, 610059, China; ²Key Laboratory of Metallogenic Prediction of Nonferrous Metals and Geological Environment Monitoring, Ministry of Education, School of Geosciences and Info-Physics, Central South University, Changsha 410083, China; ³Dipartimento di Geoscienze, Università degli studi di Padova, Via G. Gradenigo 6, 35131 Padova, Italy; ⁴Institute of Mineral Engineering, Hunan University of Science and Technology, Xiangtan, 411201, China; ⁵Guangxi Key Laboratory of Hidden Metallic Ore Deposits Exploration, and College of Earth Science, Guilin University of Technology, Guilin 541004, China and ⁶School of Earth Sciences, China University of Geosciences, Wuhan, 430074, China

Abstract

The study of enclaves in granitic plutons provides fundamental information on the petrogenesis of their host rocks. Here we combine U–Pb zircon ages, petrography, geochemistry and Nd–Hf isotope composition to investigate the origin of dioritic–granodioritic enclaves and their host granodiorites and biotite granites in the Xuehuading–Panshanchong area, which is a pivotal site to study the Palaeozoic intracontinental orogenic processes of the South China Block. Obtained ages indicate that the host rocks were formed in early Silurian time (*c.* 432 Ma). The enclaves are fine grained, but with mineral assemblages similar to their hosts and contain amphibole, biotite and plagioclase. All rocks have fractionated rare earth element patterns ($(La/Yb)_N = 2.86–8.16$), except for one biotite granite that has a concave rare earth element pattern ($(La/Yb)_N = 1.50$). Most rocks are depleted in Ta–Nb–Ti, and have negative Eu anomalies and $\epsilon Nd(t)$ (–8.86 to –5.75) and zircon $\epsilon Hf(t)$ (–13.30 to –4.11, except for one, –39.08). We interpret that the enclaves were formed at the borders of magma-ascending conduits, where the mafic mineral crystallization was enhanced by rapid cooling. Conversely, the biotite granites were produced by fractional crystallization from a related granodiorite magma. The sample with a concave rare earth element pattern may have been influenced by hydrothermal fluid–melt interaction. Geochemical modelling suggests that the granodiorites were likely generated by disequilibrium melting of heterogeneous amphibolites in the middle–lower crust. Considering the geological data for the Palaeozoic magmatic rocks in the South China Block, we propose that the Xuehuading–Panshanchong magmatism was likely triggered by piecemeal removal of the thickened lithospheric root and subsequent thermal upwelling of mantle, without a mantle-derived magma contribution to the granites.

1. Introduction

Integrated studies of enclaves and their host and associated rocks can provide pivotal information to better understand granite petrogenesis and evolution. Enclaves are dark, fine-grained inclusions commonly found in granitic rocks and have an important role in elucidating the source of the host granitic rocks, magmatic processes and crustal evolution (Didier, 1973; Vernon, 1984; Bacon, 1986; Holden *et al.* 1987; Waight *et al.* 2001; Donaire *et al.* 2005; Shellnutt *et al.* 2010; Sun *et al.* 2010; Wang *et al.* 2012; Farner *et al.* 2014; Zhang *et al.* 2016; Rong *et al.* 2017). The models proposed to explain the formation of enclaves can be divided into open and closed (cognate) systems. The open system is characterized by the presence of foreign lithic/crystal fragments or mantle-derived magma incorporated during the emplacement of the host magma, including country rock (Barbarin, 2005) or material from deeper levels of the crust (Domenick *et al.* 1983; Xu *et al.* 2006) and remnants of mingled (Browne *et al.* 2006; Karsli *et al.* 2007; Zhang *et al.* 2016) or mixed (Holden *et al.* 1987; Mass *et al.* 1997; Yang *et al.* 2007b; Chen *et al.* 2009; Sun *et al.* 2010) magmas with or without a gabbroic composition. Enclaves of the closed system may be represented by restites (Chappell *et al.* 1987; Chappell, 1996; Chappell & Wyborn, 2012) and/or unmelted portions of the source region

(White *et al.* 1999; Carvalho *et al.* 2017), autoliths from the early formed portions of the granitic magma with a high degree of crystal accumulation (Langmuir, 1989; Bea, 2010; Shellnutt *et al.* 2010; Niu *et al.* 2013) and aggregates from the back-reaction of peritectic mafic minerals with the host granitic melt (Rong *et al.* 2017).

Among these, the most popular interpretation has always emphasized the contribution of mantle-derived magma as a material and heat source (Niu *et al.* 2013) to explain the various isotopic features in enclaves–host rocks and certain minerals (Yang *et al.* 2007b; Sun *et al.* 2010). However, there are large granitic provinces in which the igneous rocks are predominantly felsic and the mafic ones, if present, are usually minor (Sheth, 2007; Alves *et al.* 2009; Huang *et al.* 2015). In such cases, their origin is not related to mantle input but rather to different processes. For instance, chemical and isotopic variations may also be influenced by source nature and melting conditions (Hogan & Sinha, 1991; Hammouda *et al.* 1996; Knesel & Davidson, 1996; Ayres & Harris, 1997; Davies & Tommasini, 2000; Zeng *et al.* 2005a,b; Tang *et al.* 2014; Huang *et al.* 2015; Hammerli *et al.* 2018). Therefore, it is necessary to re-evaluate the petrogenesis of enclaves and their host granitic rocks in some large granitic provinces.

Magma chambers are active systems where many evolutionary processes could occur including fractional crystallization, assimilation and magma mixing (Hawkesworth *et al.* 2000, 2004). Even if crystal fractionation of less-evolved magmas is an important mechanism to generate evolved magmas in closed magmatic systems, there are also various degrees of magma evolution (e.g. Miller, 1985). Granitic rocks are extensively exposed in the South China Block (SCB), and these rocks are often composed of a series of rock units (e.g. granodiorite, biotite granite and leucogranite) (Wang *et al.* 2014; Huang *et al.* 2015). In such igneous complexes, the evolved rock types generally show clear late intrusive contacts towards the other rock units (e.g. Wang *et al.* 2014). Therefore, it is important to clarify whether or not fractional crystallization is the dominant cause of the silicic magma evolution.

This study investigates the origin of enclaves and their host granitic rocks in the middle Palaeozoic Xuehuading (XHD) and Panshanchong (PSC) granitic plutons, exposed or drilled in the SCB (Fig. 1b). We present field and petrographic observations, U–Pb zircon dating, mineral composition (major and trace elements) and Nd–Hf isotopic data to reveal the ages, sources and crystallization conditions of the enclaves and host rocks, and their implications for the crustal evolution of the SCB during intracontinental orogenic processes (e.g. Ou *et al.* 2019). The results show that the variable isotopic signatures of the enclaves, host rocks and certain minerals were not only controlled by their heterogeneous source but also influenced by the disequilibrium melting process.

2. Geological setting

2.a. Regional geology

The SCB is composed of the Yangtze Block in the west and the Cathaysia Block in the east (Fig. 1a), which were separated by the Jiangshan–Shaoxing Fault (JSF), verified by Neoproterozoic ophiolites, arc-type granite and high-pressure/low-temperature blueschists (Li *et al.* 2008, 2009; Yao *et al.* 2014). However, the southward extension of the JSF is uncertain owing to poor exposure and younger tectonic modifications (Li *et al.* 2010; Wang *et al.* 2013a). More and more geochemical and geophysical evidence supports the Chenzhou–Linwu Fault (CLF) as being the southwestern boundary between the two blocks (Fig. 1b; Zhang &

Wang, 2007; Zhang *et al.* 2012; Wang *et al.* 2013a). Previous studies have confirmed that the Yangtze and Cathaysia blocks have been a single block since their collision in Neoproterozoic time (Wang *et al.* 2006; Li *et al.* 2008).

The basement of the Yangtze Block is predominantly composed of Proterozoic metamorphic rocks (Chen & Jahn, 1998) and a small amount of Archaean rocks known as the Kongling Complex (Gao *et al.* 1999; Qiu *et al.* 2000). In the Cathaysia Block, no Archaean basement has been reported; there are some Palaeoproterozoic granites and metasedimentary and volcanic rocks exposed in the northeastern Wuyi dome area (Fig. 1b; Yu *et al.* 2009, 2010). The middle Palaeozoic faults and related folds are exposed in the southeastern SCB, i.e. east of the Anhua–Luocheng Fault (Fig. 1b). The Eastern Yangtze Block only underwent greenschist metamorphism and thin-skinned thrust tectonics (Charvet *et al.* 2010); however, the Cathaysia Block is characterized by both thin- and thick-skinned structures and greenschist- to granulite-facies metamorphism (Faure *et al.* 2009; Charvet *et al.* 2010). Middle Palaeozoic igneous rocks are important products of the Phanerozoic magmatism to the east of the Anhua–Luocheng Fault in the eastern SCB (Fig. 1b).

An evident geological feature of the SCB is the extensive occurrence of Phanerozoic igneous rocks dominated by granites (Fig. 1b), which are regarded as one of the biggest granitic provinces worldwide (Zhang *et al.* 2012; Wang *et al.* 2013a; Huang *et al.* 2015). These granites mainly occur to the east of the Anhua–Luocheng Fault (including the Eastern Yangtze Block and Cathaysia Block; Fig. 1b) and were formed in response to three major events, namely the Kwangsian (middle Palaeozoic), Indosinian (Triassic) and Yanshanian (Jurassic–Cretaceous) tectonothermal events (Wang *et al.* 2013a). Middle Palaeozoic igneous rocks in the SCB are dominated by calc-alkaline granites (Wang *et al.* 2013a; Ou *et al.* 2019) with minor contemporaneous basaltic rocks (Yao *et al.* 2012; Wang *et al.* 2013b; Zhong *et al.* 2013, 2014; Jia *et al.* 2017). Recent studies have shown a strong petrological contrast between the Eastern Yangtze Block and Cathaysia Block (Wang *et al.* 2013a; Ou *et al.* 2019). For instance, after the magmatic age peak, a remarkable juvenile component is well observed in the Cathaysia Block granitic rocks but not in the Eastern Yangtze Block (c. 424 Ma for the Eastern Yangtze Block and c. 438 Ma for the Cathaysia Block; Ou *et al.* 2019). Only minor mafic magmatic rocks (including mafic microgranular enclaves) occur in the Eastern Yangtze Block (including Daning lamprophyres (c. 432 Ma) (Jia *et al.* 2017) and Taoyuan hornblende gabbros (c. 409 Ma) (Zhong *et al.* 2013); Fig. 1b), exposed near the JSF–CLF, which penetrated the Moho (Zhang & Wang, 2007).

2.b. Granitic rocks and enclaves from Xuehuading (XHD) and Panshanchong (PSC)

The study area is situated in southwestern Hunan Province, Eastern Yangtze Block, which is located west of the CLF (Fig. 1b). Most of the faults in the study area show a northeastern strike (Fig. 1c, d). The XHD granitic pluton is located southwest of Ningyuan county and has an exposed area of ~109 km² (Fig. 1c). The pluton intruded early Palaeozoic metamorphic rocks (Fu *et al.* 2004; Cheng *et al.* 2009) and has its long axis trending NNW. Moreover, it is intruded by Late Jurassic (c. 153 Ma) granites to the east (Liu *et al.* 2019) (Fig. 1c).

The XHD granitic rocks consist of dark grey granodiorite (Fig. 2a), grey biotite granite (Fig. 2b) and dark grey microgranular enclaves with sizes ranging from 5 to 10 cm (Fig. 2c, d).

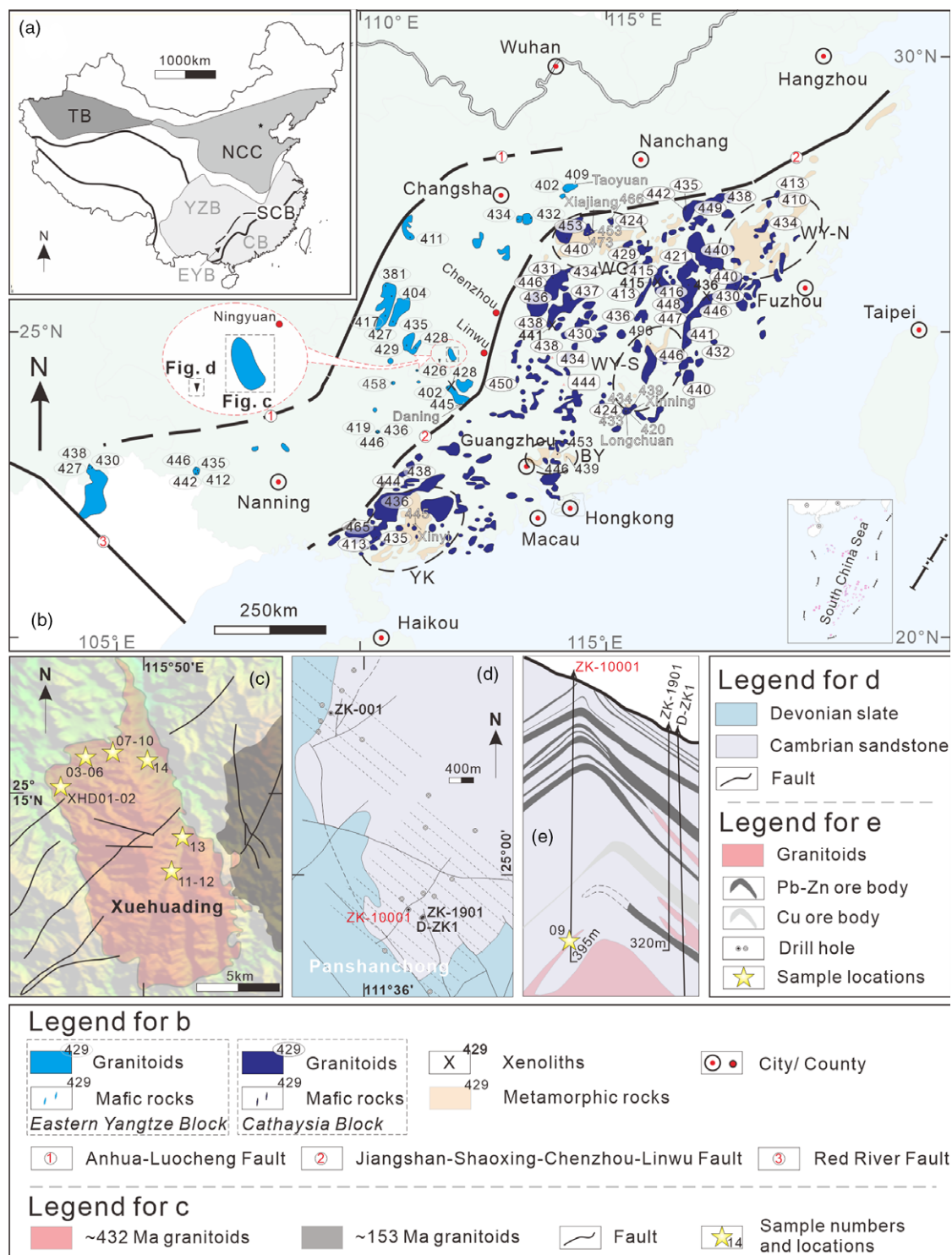


Fig. 1. (Colour online) (a) Simplified map showing the main tectonic units of China. Abbreviation: SCB – South China Block; YZB – Yangtze Block; CB – Cathaysia Block; NCC – North China Block; TB – Tarim Block. (b) Schematic map showing the distribution of the middle Palaeozoic magmatic rocks in the South China Block. Abbreviation: YK – Yunkai dome; BY – Baiyun dome; WY-S – southern Wuyishan dome; WY-N – northern Wuyishan dome; WG – Wugongshan dome. The number near the magmatic rocks represents the U–Pb zircon ages from previous works based on Ou *et al.* (2019). (c) Geological map of the Xuehuading (XHD) granitic pluton. (d) Geological map and (e) cross-section of prospecting line of the Panshanchong (PSC) area.

Granodiorites occur together with biotite granites (samples 11 and 12) in the same outcrop (Fig. 1c); however, there is no clear contact between the two rock types. The enclaves are all hosted in granodiorite. Most rocks in XHD are granodiorites dominated by plagioclase (30–40% in modal proportion), K-feldspar (15–20%), quartz

(20–30%), amphibole (1–5%) and biotite (5–15%) (Fig. 2e). The biotite granite samples in XHD are hornblende free, and dominated by plagioclase (20–30%), K-feldspar (20–25%), quartz (30–40%) and biotite (5–15%) (Fig. 2f). Enclaves are dioritic to granodioritic in composition, with main mineral assemblages of

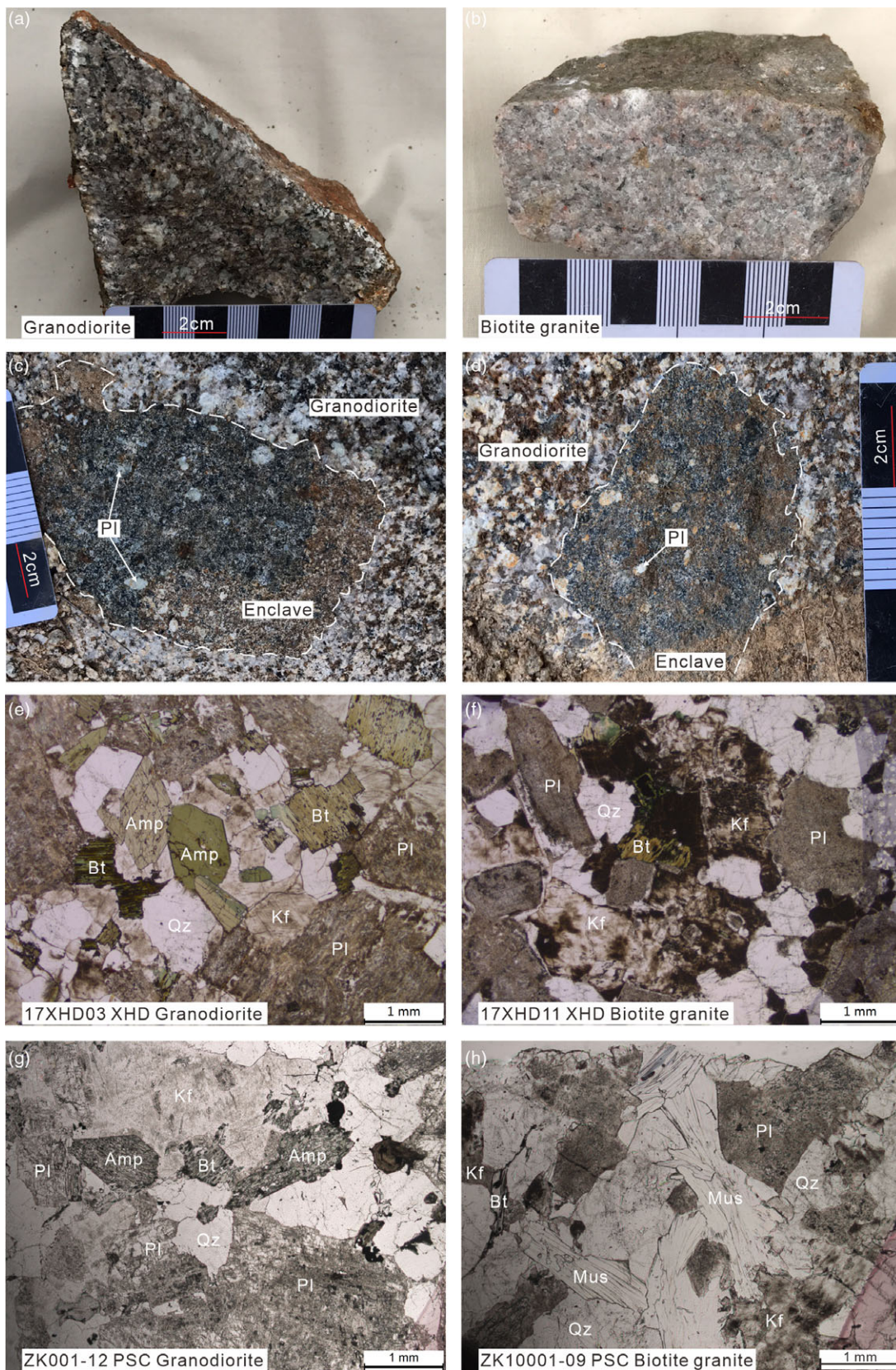


Fig. 2. (Colour online) Representative photographs and photomicrographs of host granitic rocks and enclaves investigated in this study. Hand-specimens of (a) medium-grained black grey granodiorite, (b) grey biotite granite and (c, d) fine-grained dark grey enclaves. (e) Granodiorite with light green-euhedral amphibole in XHD (sample 17XHD03). (f) Biotite granite in XHD (sample 17XHD11). (g) Granodiorite with euhedral to subhedral amphibole in PSC (sample ZK001-12). (h) Biotite granite with elongated muscovite in PSC (sample ZK10001-09). Abbreviations: Amp – amphibole; Bt – biotite; Kf – K-feldspar; Mus – muscovite; Pl – plagioclase; Qz – quartz.

plagioclase (34–65 %), biotite (12–15 %) and amphibole (2–6 %); a few samples also have K-feldspar (2–21 %) and quartz (8–22 %) (Cheng *et al.* 2009). In XHD, all the enclaves within the granodiorites commonly occur as lobate shapes and do not show evidence of reaction with the host magma (Fig. 2c, d). Nevertheless, there are some feldspar crystals that appear to cross the boundaries into the enclaves (Fig. 2c, d).

The PSC pluton is a concealed body only exposed by drilling during prospecting works, and it is 40 km away from XHD (Fig. 1d). Its size is not entirely known, but it has been interpreted to be related to the XHD pluton because of their similar rock associations and ages (see Section 4 below). Both plutons intrude the Cambrian sandstone or sandy slate (Cheng *et al.* 2009) (Fig. 1c, d).

In PSC, there are also two types of granitic rocks: granodiorite and biotite granite samples from the granitic pluton and dyke, respectively. Biotite granites occur towards the upper part, and granodiorites are the dominant rock type towards the lower part based on the drilling data in the PSC area (Fig. 1e). There are no enclaves found in the PSC samples. As a whole, the studied PSC samples show similar mineral assemblages to those from XHD (Fig. 2g, h). However, the biotite granite samples from PSC also contain muscovite and relatively lower modal proportions of biotite compared to the biotite granites from XHD (Fig. 2h). Some biotite grains show transitional optical characteristic between biotite and muscovite (left part of Fig. 2h).

3. Samples and analytical methods

3.a. Samples

We selected 17 representative samples (including two duplicates) for analysis: 13 granodiorites and 2 biotite granites from XHD, and one sample of each granodiorite and biotite granite from PSC. Even if we found an outcrop of microgranular enclaves hosted in the granodiorites during the fieldwork (Fig. 2c, d), we were unable to collect samples fresh enough. In order to remediate this problem, we used data from a previous study (Cheng *et al.* 2009), which investigated enclaves exposed in the same outcrop from which we collected our samples (online Supplementary Material Fig. S1 and site XHD14 in Fig. 1c).

3.b. Whole-rock major- and trace-element contents and Nd isotopes

After petrographic examinations, the least-altered whole-rock samples were selected for geochemical and Nd isotopic analyses. The rocks were sawn into small chips, ultrasonically cleaned in distilled water, and subsequently dried and handpicked to remove any visible contamination (e.g. weathered surfaces). Then the rocks were crushed and ground in an agate mortar and subjected to 1 minute of milling each time, three times (total milling time around 3 minutes), and the resulting powders were used for analyses of major and trace elements and Nd isotopes at the Guangxi Key Laboratory of Hidden Metallic Ore Deposits Exploration, Guilin University of Technology (GKLaHMODE GLUT), Guilin and Nanjing FocuMS Technology Co. Ltd (FocuMS), respectively. Major-element oxides were analysed using a Rigaku RIX 2000 X-ray fluorescence spectrometer at GLUT on fused glass beads. Calibration lines used in quantifications were produced by bivariate regression of data from 36 reference materials encompassing a wide range of silicate compositions. The analytical results for the USGS reference standards (GSR-1, GSR-2 and GSR-3) indicate that the analytical uncertainties were generally less than 2%.

Trace elements (including rare earth elements (REEs)) were analysed using a Perkin-Elmer Sciex ELAN 6000 inductively coupled plasma mass spectrometer (ICP-MS). Analytical procedures are identical to those described in Li *et al.* (2006). USGS reference standards (BHVO-2, AVG-2, GSR-1, GSR-2, GSR-3, W-2, SY-4, GSD-9 and SARM-4) were chosen as external calibration standards for calculating the elemental concentrations in the measured samples. The total procedure blank was treated in the same way as the samples, and was corrected in all of the samples and reference standards. Analytical precision and accuracy are better than 3%.

Whole-rock Nd isotopic compositions of selected samples were determined using a Nu Plasma II multi-collector (MC)-ICP-MS at FocuMS. Analytical procedures are identical to those described in Li *et al.* (2004) and Wei *et al.* (2002). Sample powders were first dissolved in distilled acetic acid (10 %) for 24 h at 60 °C, and then the residues were dissolved in Teflon beakers with HF + HNO₃, and separated by conventional cation-exchange techniques. Neodymium isotopes were all purified from the same digestion solution by two-step column chemistry. The first exchange column combined with Bio-Rad AG 50W-X8 and Sr Spec resin was used to separate Sr, REEs and Pb from the sample matrix. Neodymium was separated from the other REEs on the second column with Ln Spec-coated Teflon powder. All the measured ¹⁴³Nd/¹⁴⁴Nd ratios were normalized to ¹⁴⁶Nd/¹⁴⁴Nd = 0.7219.

3.c. Zircon U–Pb ages and Hf isotope analyses

Zircons were separated using conventional heavy liquid and magnetic separation techniques, purified by hand-picking under a binocular microscope, mounted in an epoxy resin disc and then polished. Their internal morphology was carefully examined and target sites were selected using cathodoluminescence (CL) images obtained at FocuMS with a JSM-6510 scanning electron microscope attached to a Gatan CL detector prior to U–Pb and Lu–Hf isotope analyses.

Laser-ablation (LA)-ICP-MS U–Pb ages and trace-element concentrations in zircon were analysed simultaneously using an Agilent 7700x ICP-MS connected to an attached Analyte Excite laser-ablation system with a spot diameter of 35 µm at 8 Hz repetition rate for 40 s (equating to 320 pulses) at FocuMS. Zircon 91500 (Liu *et al.* 2010) was used as the standard, and standard silicate glass NIST 610 (Liu *et al.* 2010) was used to optimize the machine. Analyses were acquired with a beam diameter of 35 µm. Raw count rates for ²⁹Si, ²⁰⁴Pb, ²⁰⁶Pb, ²⁰⁷Pb, ²⁰⁸Pb, ²³²Th and ²³⁸U were collected and U, Th and Pb concentrations were calibrated using ²⁹Si as the internal calibrant and NIST 610 as the reference material. Details of the analytical techniques are described by Wu *et al.* (2006). Common Pb was corrected by ComPbCorr#3 151 (Andersen, 2002) for those samples with common ²⁰⁶Pb > 1%. The U–Pb ages were calculated using the ICPMSDataCal (version 8.0) recommended by Liu *et al.* (2010) and Isoplot/Ex 3 software (Ludwig, 2003). During the analyses in this study, GJ-1 and Plešovice analysed as unknown samples yielded weighted ²⁰⁶Pb–²³⁸U ages of 600 ± 4 Ma (2σ, MSWD = 0.017, n = 12) and 336.2 ± 4 Ma (2σ, MSWD = 0.2, n = 5), respectively, which is in good agreement with their recommended ages (600 ± 5 Ma, GJ-1, Jackson *et al.* 2004; and 337.1 ± 0.4 Ma, Plešovice, Sláma *et al.* 2008). The standard zircon 91500 yielded a weighted ²⁰⁶Pb–²³⁸U age of 1062 ± 5 Ma (2σ, MSWD = 0.002, n = 20), which is in good agreement with the recommended age (²⁰⁶Pb–²³⁸U = 1062.4 ± 0.4 Ma, ²⁰⁷Pb–²⁰⁶Pb = 1065.4 ± 0.3 Ma) within errors (Wiedenbeck *et al.* 1995).

In situ zircon Hf isotope measurements were subsequently done using a Neptune Plus MC-ICP-MS with a beam size of 44 μm and laser pulse frequency of 8 Hz with age determinations at the GKLaHMODE GLUT. The detailed analytical technique and data correction procedure are described by Wu *et al.* (2006). The isobaric interference of ^{176}Lu on ^{176}Hf is negligible owing to the extremely low $^{176}\text{Lu}/^{177}\text{Hf}$ in zircon (normally < 0.002). The standard zircon GJ-1 was used for external corrections. During the analyses, the $^{176}\text{Hf}/^{177}\text{Hf}$ ratio of the standard zircon GJ-1 was 0.282028 ± 0.000004 (2SD, MSWD = 1.5, $n = 17$), consistent with the recommended values (0.282000 ± 0.000005) within analytical errors (Morel *et al.* 2008; Geng *et al.* 2011).

3.d. Mineral compositions

All mineral analyses were carried out at the State Key Laboratory of Isotope Geochemistry, Guangzhou Institute of Geochemistry, Chinese Academy of Sciences with a JEOL JXA-8100 Superprobe. Operating conditions were as follows: 15 kV accelerating voltage, 20 nA beam current, 1–2 μm beam diameter, 10 second counting time and ZAF correction procedure for data reduction. The analytical procedures were described in detail by Huang *et al.* (2007).

4. Results

4.a. Zircon U–Pb ages

The studied granitic samples were selected for zircon dating (Fig. 3; online Supplementary Material Table S1), including three granodiorites (17XHD06 and 17XHD08 from XHD; ZK001-12 from PSC) and one biotite granite (17XHD12 from XHD). Most of the analysed zircons are prismatic (80–400 μm in length and 80–100 μm in width) with well-developed pyramidal faces (Fig. 3a). Most of the CL images show micro-scale oscillatory zoning (Fig. 3a) and exhibit Th/U ratios mostly between 0.1–1 (0.25–0.68, 0.25–0.60, 0.29–1.46 and 0.22–0.87 for samples 17XHD06, 17XHD08, 17XHD12 and ZK001-12, respectively) (online Supplementary Material Table S1) suggesting a magmatic origin for the zircons (Belousova *et al.* 2002). There are also some grains with weak zoning in sample 17XHD08; furthermore, some of them display cores with high U contents, as shown by their very bright CL images (Fig. 3a). The results of the LA-ICP-MS U–Pb zircon analyses for the studied samples are listed in online Supplementary Material Table S1 and illustrated on a concordia plot in Figure 3b–e.

Nineteen analyses of zircons from sample 17XHD06 yield a ^{206}Pb – ^{238}U single age population of between 430 and 436 Ma, with a weighted mean age of 432.1 ± 2.5 Ma (mean square weighted deviation, MSWD = 0.037) and concordant age of 431.9 ± 2.6 Ma (MSWD = 0.023) (Fig. 3b). Spot 06 (in sample 17XHD06) gives a ^{206}Pb – ^{238}U age of 648 Ma, which suggests that some zircons were likely inherited or entrained from the wall rocks during granitic magma emplacement (Fig. 3b; online Supplementary Material Table S1). For zircons from sample 17XHD08, 17 analyses resulted in a weighted mean age and concordant age of 431.7 ± 2.4 Ma (MSWD = 0.03) and 431.7 ± 2.8 Ma (MSWD = 0.028), respectively (Fig. 3c). There are two inherited zircons (spots 06 and 18 in sample 17XHD08) with ^{206}Pb – ^{238}U ages of 514 ± 7 Ma and 1600 ± 15 Ma, respectively (online Supplementary Material Table S1). These ages also occur in the core of some grains with a core–rim texture (Fig. 3a). Spot 15 (in sample 17XHD08) yielded a younger ^{206}Pb – ^{238}U age

of 408 ± 4 Ma, probably caused by its mineral inclusions (Fig. 3a; online Supplementary Material Table S1). Seventeen analyses of zircons from sample 17XHD12 yield a weighted mean ^{206}Pb – ^{238}U age of 432.0 ± 2.3 Ma (MSWD = 0.05) and a concordant age of 431.7 ± 3.3 Ma (MSWD = 0.063) (Fig. 3d; online Supplementary Material Table S1). In sample 17XHD12, spots 08 and 09 produced younger ^{206}Pb – ^{238}U ages of 383 ± 4 Ma and 423 ± 6 Ma, respectively. These younger ages were probably caused by the high common lead contents of those grains ($f_{206} = 0.65\%$ for spot 08 and 2.19% for spot 09) (online Supplementary Material Table S1). Seventeen analyses of zircons from sample ZK001-12 resulted in a weighted mean ^{206}Pb – ^{238}U age of 431.9 ± 2.3 Ma (MSWD = 0.046) and concordant age of 431.6 ± 2.4 Ma (MSWD = 0.25) (Fig. 3e; online Supplementary Material Table S1). The age data for two spots (spot 09 and 16) in sample ZK001-12 were deleted owing to their unusual test errors (online Supplementary Material Table S1). Spot 21 (in sample ZK001-12) produced a younger ^{206}Pb – ^{238}U age of 424 ± 4 Ma, probably caused by Pb loss (Fig. 3e; online Supplementary Material Table S1). Thus, the consistent U–Pb zircon age data for three samples suggest the XHD and PSC granitic rocks were formed in late early Silurian time (*c.* 432 Ma).

4.b. Mineral chemistry

Representative electron microprobe analyses of biotite, amphibole, plagioclase, K-feldspar and Fe–Ti oxides from the granodiorites and biotite granites are given in online Supplementary Material Table S2. The *in situ* trace-element data for the magmatic zircons are presented in online Supplementary Material Table S3.

4.b.1. Biotite

The composition of biotite crystals from the XHD and PSC granodiorites lie within the Mg-biotite to Fe-biotite field based on the classification of Foster (1960) (Fig. 4a), characterized by relatively moderate MgO (9.10–12.07 wt %) and FeO^{T} (17.85–24.07 wt %) contents, with $\text{Mg}/(\text{Mg} + \text{Fe}^{2+})$ (in atoms per formula unit (apfu)) ranging from 0.44 to 0.60. The $10 \times \text{TiO}_2 - (\text{FeO} + \text{MnO}) - \text{MgO}$ ternary diagram of Nachit *et al.* (2005) was used to discriminate magmatic or primary biotite from secondary or re-equilibrated biotite (Fig. 4b). On this diagram, all of the biotite crystals plot in the field of primary biotite, consistent with their euhedral to subhedral shapes (Fig. 2e–h). In contrast, muscovite crystals in the biotite granite from PSC contain low TiO_2 (0.24–0.25 wt %) and high MgO (0.76–0.92 wt %) contents, and plot in the field of secondary muscovite on the diagram of Miller *et al.* (1981) (Fig. 4c).

4.b.2. Amphibole

The classification of amphiboles is according to the International Mineralogical Association's classification scheme (Leake *et al.* 1997). All of the amphiboles in the studied granodiorites belong to the calcic group (Ca_B (1.70–1.89) > 1.50 apfu) (Fig. 4d, e inset). In the granodiorites from XHD, the amphiboles belong to the magnesiohornblende–actinolite series (with $(\text{Na} + \text{K})_A$ and $\text{Mg}/(\text{Mg} + \text{Fe}^{2+})$ (in apfu) ranging from 0.03 to 0.49 and 0.54 to 0.86 apfu, respectively; Fig. 4d) and edenite (with $(\text{Na} + \text{K})_A$ and $\text{Mg}/(\text{Mg} + \text{Fe}^{2+})$ ranging from 0.52 to 0.60 and 0.52 to 0.59 apfu; Fig. 4e). The amphibole of the granodiorites from PSC is edenite with $(\text{Na} + \text{K})_A$ and $\text{Mg}/(\text{Mg} + \text{Fe}^{2+})$ of around 0.72 and 0.54, respectively (Fig. 4e). Almost all amphibole grains plot in the felsic-magma derived fields, except for a few grains (mostly actinolite, Fig. 4d) that underwent later alteration (Fig. 4f).

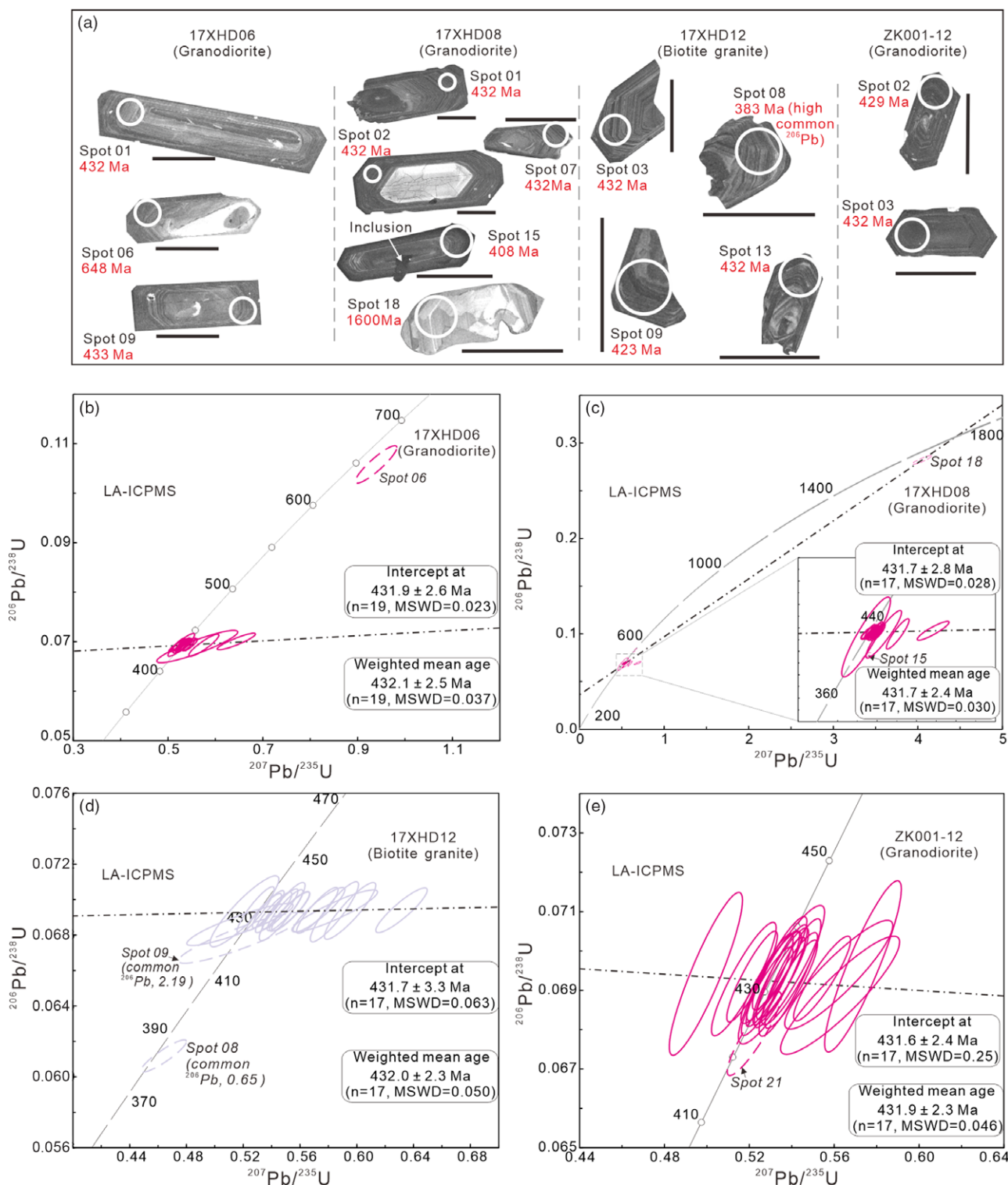


Fig. 3. (Colour online) (a) Representative cathodoluminescence images and (b–e) U–Pb concordia diagrams of zircons from the studied granitic rocks. The solid black circles on zircon CL images indicate the locations of U–Pb age sites. Scale bars and circles are 100 and 35 μm , respectively.

4.b.3. Feldspars

The plagioclase grains exhibit euhedral to subhedral shapes and are characterized below in terms of mole fraction of anorthite (An_X). Significant compositional zoning of single crystals has not been observed; however, they show a wide compositional range, including andesine (An_{36-38}), oligoclase (An_{12-24}) and albite (An_{0-4}) (Fig. 4g),

related to different stages of crystallization of the host magma. On the whole, the plagioclase grains from the granodiorites show a wide compositional range, while the ones from the biotite granites display lower An_X values (Fig. 4g). All of the K-feldspar grains plot in the field of sanidine, with a composition of Or_{88-98} (mole fraction of orthoclase, Or_X) (Fig. 4g).

4.b.4. Fe–Ti oxides

Representative analyses of Fe–Ti oxides are given in online Supplementary Material Table S2. All of the Fe–Ti oxides show low TiO₂ contents (0.25–0.27 wt %) and are mostly magnetite (TiO₂ ≤ 5 wt %).

4.b.5. Zircon

All magmatic zircon crystals exhibit wide variations in composition, ranging from 0.02 to 26.18 (ppm) La contents, 0.9 to 476 (Sm/La)_N and 1.2 to 113 Ce/Ce* (online Supplementary Material Table S3). In the discriminant plots for magmatic and hydrothermal zircons from Hoskin (2005), all of the studied zircons show a well-marked trend from magmatic to hydrothermal zircon (Fig. 5a, b). Most of the studied zircons exhibit enrichment of heavy REEs (HREEs) relative to light REEs (LREEs), strong positive Ce anomalies and relatively small negative Eu anomalies (Fig. 5c–f). Moreover, the REE patterns of some zircon grains show higher abundances of the REEs, flatter LREE patterns and smaller Ce anomalies of various degrees (Fig. 5c–f). These unusual zircon REE patterns in granitic rocks have been ascribed to the influence of zircon-saturated aqueous fluid (Fig. 5c, e, f; Hoskin, 2005).

4.c. Whole-rock major and trace elements

Whole-rock major- and trace-element data of the granitic rocks are provided in online Supplementary Material Table S4, including 11 granodiorites, 2 biotite granites and 3 enclaves (Cheng *et al.* 2009) from XHD, and one granodiorite and one biotite granitic dyke from PSC. All of the major-element contents were normalized to an anhydrous basis. Granitic rocks from XHD and PSC show relatively higher SiO₂ and K₂O, but lower TiO₂, Al₂O₃, Fe₂O₃^T, MgO, CaO, P₂O₅ and MnO than the enclaves (except for one sample) from XHD (Fig. 6). Overall, the studied samples combined with the enclaves show a general trend of decreasing TiO₂, Fe₂O₃^T, MgO and P₂O₅ with increasing SiO₂ (Fig. 6). All of them plot in the field of high-K calc-alkaline rocks (Fig. 6f) on the K₂O–SiO₂ classification diagram from Peccerillo & Taylor (1976).

All of the studied granitic samples show fractionated chondrite-normalized (Sun & McDonough, 1989) REE patterns ((La/Yb)_N = 2.86–8.16) with strong negative Eu anomalies (Eu/Eu* = 0.24–0.71) (Fig. 7a), except the biotite granite sample from PSC (~1.50 and 1.76 (La/Yb)_N and Eu/Eu*, respectively). The enclaves show similar chondrite-normalized REE patterns to the granodiorites (Fig. 7a). Overall, the granodiorites have relatively flat HREE patterns ((Dy/Yb)_N = 0.93–1.50), but there is a concave-upward trend between the medium REEs and HREEs in the biotite granites of XHD ((Dy/Yb)_N = 0.70–0.75) and PSC ((Dy/Yb)_N ~0.57). Moreover, the biotite granite from PSC shows much lower LREE contents than the other rocks (Fig. 7a). On a primitive mantle-normalized (Sun & McDonough, 1989) multi-element variation diagram, all studied samples show pronounced negative Nb–Ta, Ti and Sr anomalies and a positive Pb anomaly (Fig. 7b).

4.d. Whole-rock Nd isotopes

The whole-rock Nd isotope data for the XHD and PSC granitic rocks are reported in online Supplementary Material Table S4. All of the studied granitic rocks have negative εNd(t) values (–8.86 to –6.85) similar to their enclaves (–7.85 to –7.73) except for one sample (–5.75); moreover, the values are relatively lower than the contemporary (c. 432 Ma) Daning lamprophyres (–6.32 to –6.26) (Jia *et al.* 2017) from the Eastern Yangtze Block (Fig. 8a;

online Supplementary Material Table S4). Furthermore, the Nd isotopic ratios of the studied samples are consistent with the Archaean amphibolites (Gao *et al.* 1999; Zhang *et al.* 2006) from the Yangtze Block (Fig. 8a). However, they are lower than those of Early Devonian (c. 409 Ma) Taoyuan hornblende gabbros (Zhong *et al.* 2013) in the Eastern Yangtze Block (Fig. 8a).

4.e. Hf isotopes in zircon

The results of the *in situ* Hf isotope analyses of the zircons from the studied granitic rocks are provided in online Supplementary Material Table S5, and shown in the diagram of εHf(t) values versus U–Pb ages (Fig. 8b). Most of the magmatic (c. 432 Ma) zircon grains have εHf(t) values ranging from –13.30 to –4.11 (weighted average –6.10 ± 0.08), except for a grain with a strongly evolved εHf(t) value from one granodiorite (–39.08 from spot 07 in sample 17XHD08; Fig. 8b). Two inherited or xenocrystic zircon grains have εHf(t) values (–9.83 to –3.25) similar to those of related magmatic zircons, although they show much older U–Pb ages (514–648 Ma; Fig. 8b). Moreover, the zircon grains with relatively younger ages are similar to the magmatic grains, ranging from –6.99 to –5.29 (Fig. 8b). All of the magmatic zircon grains were projected into the evolution field of the Kongling Archaean amphibolites (metamorphic or inherited zircon) (Fig. 8b).

5. Discussion

5.a. Effects of alteration

The presence of abundant secondary minerals such as kaolinite and sericite replacing primary igneous phases (e.g. plagioclase) indicates that the studied granitic rocks experienced alteration, and the abundance of some mobile elements could have been modified (online Supplementary Material File 1), consistent with their variable loss on ignition (LOI) values (0.20–2.86 wt %) (online Supplementary Material Table S4). Thus, the potential effects of these processes have been assessed, and details are shown in online Supplementary Material File 1 and Figure S2. The late alteration is considered to have an insignificant effect on REEs and high-field-strength elements and the Nd isotopic ratios of the studied rocks. Conversely, the alkali metals (such as Na) were likely to have been modified by late alteration. Therefore, these mobile elements are avoided in the discussion below.

5.b. Crystallization conditions of the magma

All of the mineral-related physical–chemical results record the conditions of the magma at the time when the corresponding minerals crystallized, and they are listed in online Supplementary Material Tables S3, S4 and S6. The detailed information about how the magma crystallization conditions (*T*, *P*, oxygen fugacity and water content) were estimated is listed in online Supplementary Material File 2. All the estimated results indicate that the magma related to the studied granitic rocks experienced a normal evolutionary trend with a crystallization sequence starting with plagioclase, zircon, amphibole and biotite, to K-feldspar (Fig. 9a–c). Moreover, the occurrence of low H₂O values in the granodiorite samples (calculated using magmatic amphibole; see H₂O_{melt} in online Supplementary Material Table S6), show that the magma was initially water-undersaturated (Winter, 2009, p. 396), and as crystallization proceeded the H₂O contents increased (e.g. decreasing *P* and increasing H₂O_{melt}), finally culminating with the crystallization of amphibole.

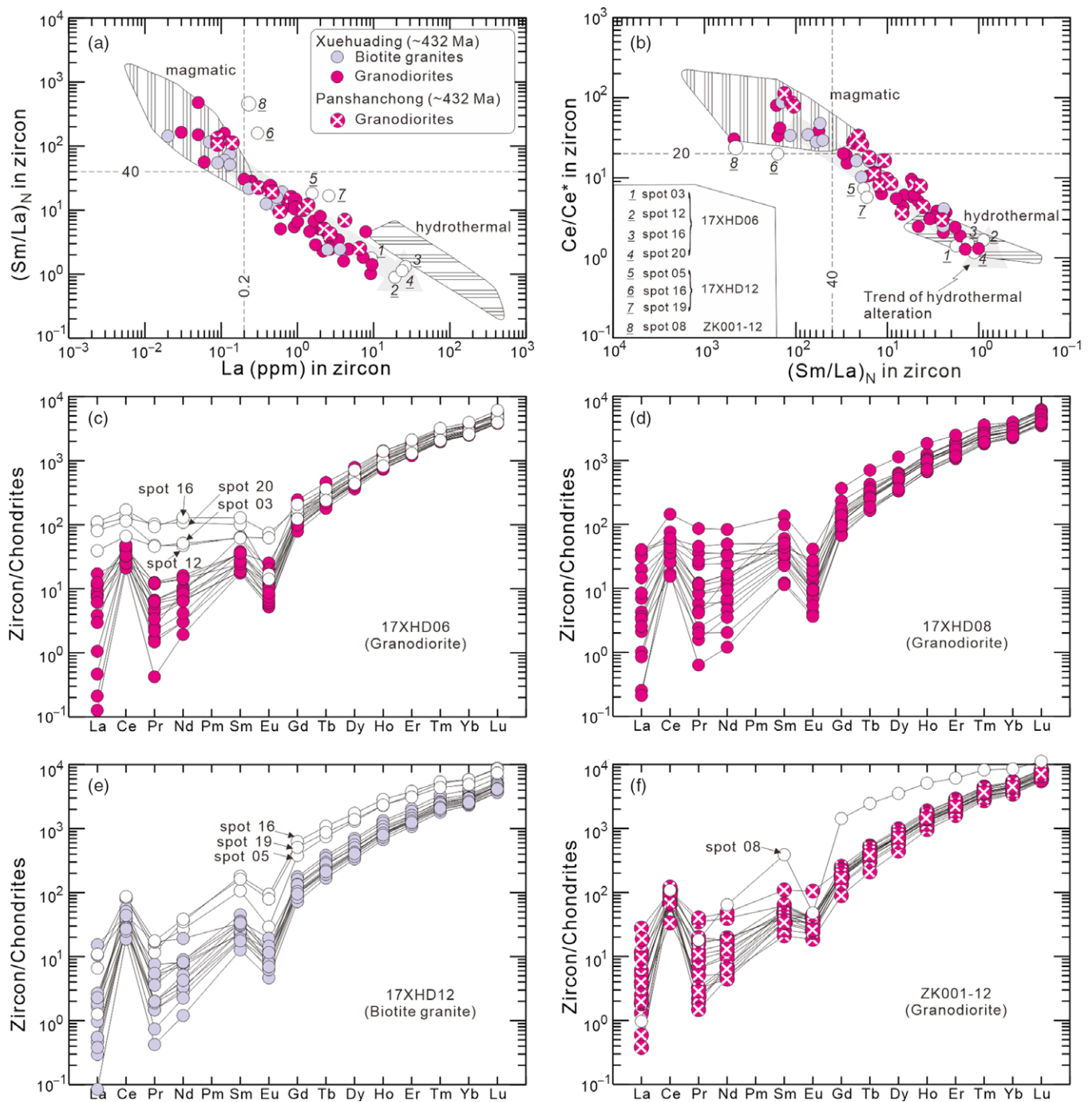


Fig. 5. (Colour online) (a, b) Discrimination diagrams for magmatic and hydrothermal zircon, and (c–f) chondrite-normalized REE patterns for magmatic zircon from the studied granitic rocks. (a) $(Sm/La)_N$ versus La (ppm). (b) Zircon Ce anomaly (Ce/Ce^*) versus $(Sm/La)_N$, ($Ce/Ce^* = Ce_N/((La_N \times Pr_N)^{0.5})$). The subscript 'N' indicates chondrite-normalized (Sun & McDonough, 1989). There are some zircon grains (numbered white circles) that deviate from the main evolutionary trend. Moreover, these zircon grains show high abundances of REEs, flatter LREE patterns and smaller Ce anomalies of various degrees, which have been ascribed to the influence of zircon-saturated aqueous fluid (Hoskin, 2005). (c) Sample 17XHD06. (d) Sample 17XHD08. (e) Sample 17XHD12. (f) Sample ZK001-12.

5.c. Petrogenesis

5.c.1. Origin of the granodiorites and biotite granites

Processes involving the addition of foreign materials, such as mixing between mantle- and crust-derived magmas (Karsli *et al.* 2007; Yang *et al.* 2007a,b), or crustal assimilation plus fractional crystallization (AFC processes; Preston *et al.* 1998; Clarke & Carruzzo, 2007; Peate *et al.* 2008), are unlikely to explain the genesis of the studied granitic rocks. The reasons are listed below. (1) The

magmatic zircons in both the granodiorites and biotite granites show similar $(Sm/La)_N$ and Ce/Ce^* ratios, and evolutionary trend from magmatic to hydrothermal zircons (Fig. 5a, b), which is consistent with evolution in a closed system; the zircons in the different rock units would display various characteristics recording different degrees of mixing if magma mixing had occurred. (2) There is a lack of a good linear compositional trend between the contemporaneous (*c.* 432 Ma) mafic magmatic rocks and studied granitic

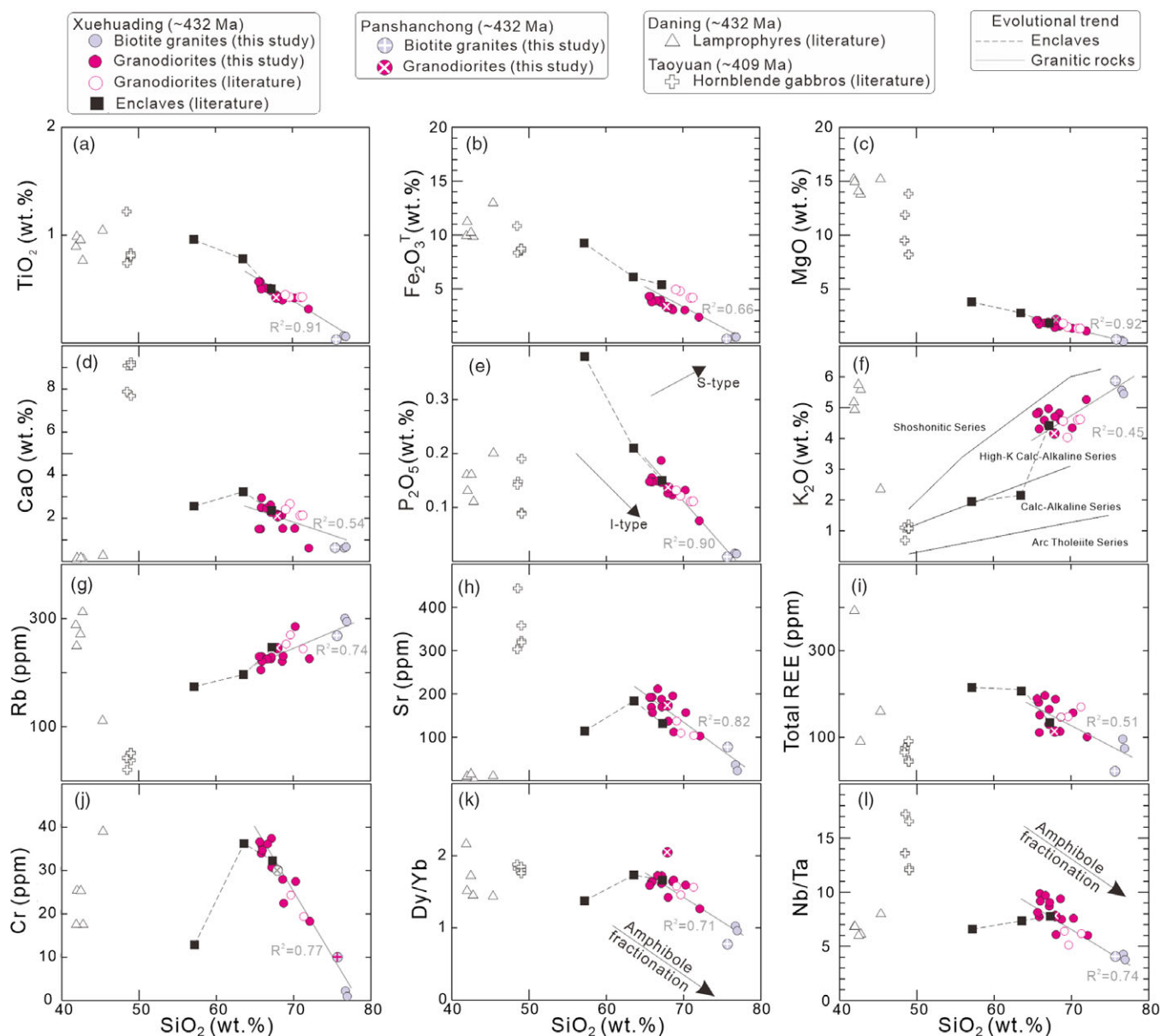


Fig. 6. (Colour online) Whole-rock Harker diagrams of (a–f) major and (g–l) trace elements for the studied granitic rocks. Data sources: Daning lamprophyres (c. 432 Ma) (Jia *et al.* 2017); Taoyuan hornblende gabbros (c. 409 Ma) (Zhong *et al.* 2013); previous data for granodiorites and enclaves (Fu *et al.* 2004; Cheng *et al.* 2009).

rocks (Fig. 6). (3) The absence of relationships between the $\epsilon\text{Nd}(t)$ and Nb/La ratios (Fig. 8a) preclude the influence of crustal assimilation (Wang *et al.* 2012).

The granitic rocks show marked decreases on the P_2O_5 versus SiO_2 diagram (Fig. 6e). This feature is a key criterion for distinguishing I-type granites from S-type granites owing to their different saturations of apatite (Chappell & White, 1992; Li *et al.* 2007). The I-type granites are mainly derived from igneous sources (e.g. Chappell & Stephens, 1988; Li *et al.* 2007). Moreover, the studied granitic rocks show similar compositions to the melts produced by partial melting of metamafic rocks (e.g. amphibolite or eclogite) at the middle to lower crustal level (Fig. 10a). In addition, all of the studied granitic rocks show single and coherent partial melting trends on the La/Yb versus La diagram (Fig. 10b). Therefore, the granitic rocks (granodiorites and biotite granites) in this study were derived from the same mafic source in the middle to lower crust. This is consistent with their similar REEs patterns, and whole-rock Nd and

zircon Hf isotopic data (Figs 7, 8). Moreover, the magmatic zircons in both the granodiorites and biotite granites show similar $(\text{Sm}/\text{La})_N$ and Ce/Ce^* ratios, and evolutionary trend from magmatic to hydrothermal zircons (Fig. 5a, b), which also indicate their similar source. However, if two rock types were derived from an identical source with different partial melting degrees, then the type with lower SiO_2 contents would show lower La/Yb ratios, owing to the higher degree of partial melting (e.g. Wang *et al.* 2006). Such a scenario is inconsistent with the samples in this study, because granodiorites and biotite granites have the similar La/Yb ratios at the same La content (Fig. 10b). Another possible interpretation is that the biotite granites are the result of fractional crystallization from the granodiorite magma. This is consistent with their evolutionary trend in Harker diagrams (Fig. 6). Moreover, plagioclase has high contents of Eu and Sr yet very low REEs and Y (McKay *et al.* 1994). Thus, negative Eu anomalies (Fig. 7a) and the positive correlations between Sr/Y ratios and Eu/Eu* (Fig. 10c) indicate plagioclase

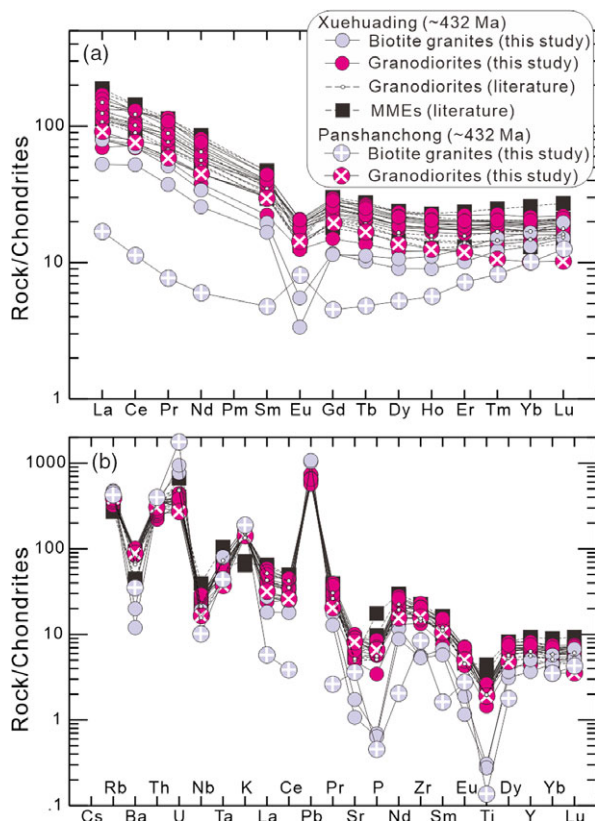


Fig. 7. (Colour online) (a) Chondrite-normalized (Sun & McDonough, 1989) rare earth element patterns and (b) primitive mantle-normalized (Sun & McDonough, 1989) spidergrams for the studied granitic rocks (this study and literature). MMEs – mafic microgranular enclaves. Data sources are as in Figure 6.

fractionation from granodiorites to biotite granites. Additionally, the separation of biotite (peraluminous mineral) would increase the $\text{SiO}_2/\text{Al}_2\text{O}_3$ but lower the V/Th ratios ($\text{Kd}(V)/\text{Kd}(\text{Th}) > 1$ of biotite; Bea *et al.* 1994) in residual melts. Hence, the negative correlation between V/Th and $\text{SiO}_2/\text{Al}_2\text{O}_3$ ratios from the granodiorites to biotite granites (Fig. 10d) suggests biotite fractionation. Therefore, variable degrees of fractional crystallization (amphibole, plagioclase and biotite) can explain the overall geochemical evolution of the studied granodiorites to biotite granites.

The scanty biotite granite in PSC shows low REE contents and a concave REE pattern (Fig. 7a). Such features are found in highly differentiated rocks affected by hydrothermal fluid–melt interaction (Maru  jol *et al.* 1990; Wu *et al.* 2004; Liu & Zhang, 2005; Dostal *et al.* 2015). This is consistent with the occurrence of hydrothermal zircons in the studied rocks (Fig. 5a, b). Accessory minerals (e.g. apatite, allanite and monazite) control the budget of REEs (Wu *et al.* 2003); therefore, such a trace-element pattern for the biotite granites could also be explained by strong fractionation of accessory minerals (Yang *et al.* 2018). Moreover, amphibole was not observed in the biotite granites. In order to quantify the role of accessory minerals, we used REE data to model this process. The results are presented in Figure 11a and online Supplementary Material Table S7. As shown in Figure 11a, the concave REE pattern of the biotite granite from PSC can be reproduced by 98% separation of the mineral assemblage ($\text{Amp}_{60}\text{Ap}_{27.5}\text{Aln}_{10}\text{Mon}_{2.5}$).

As discussed above, the primitive magma related to the studied granodiorites was most probably generated by partial melting of metamafic rocks (e.g. amphibolite or eclogite) in the middle to lower

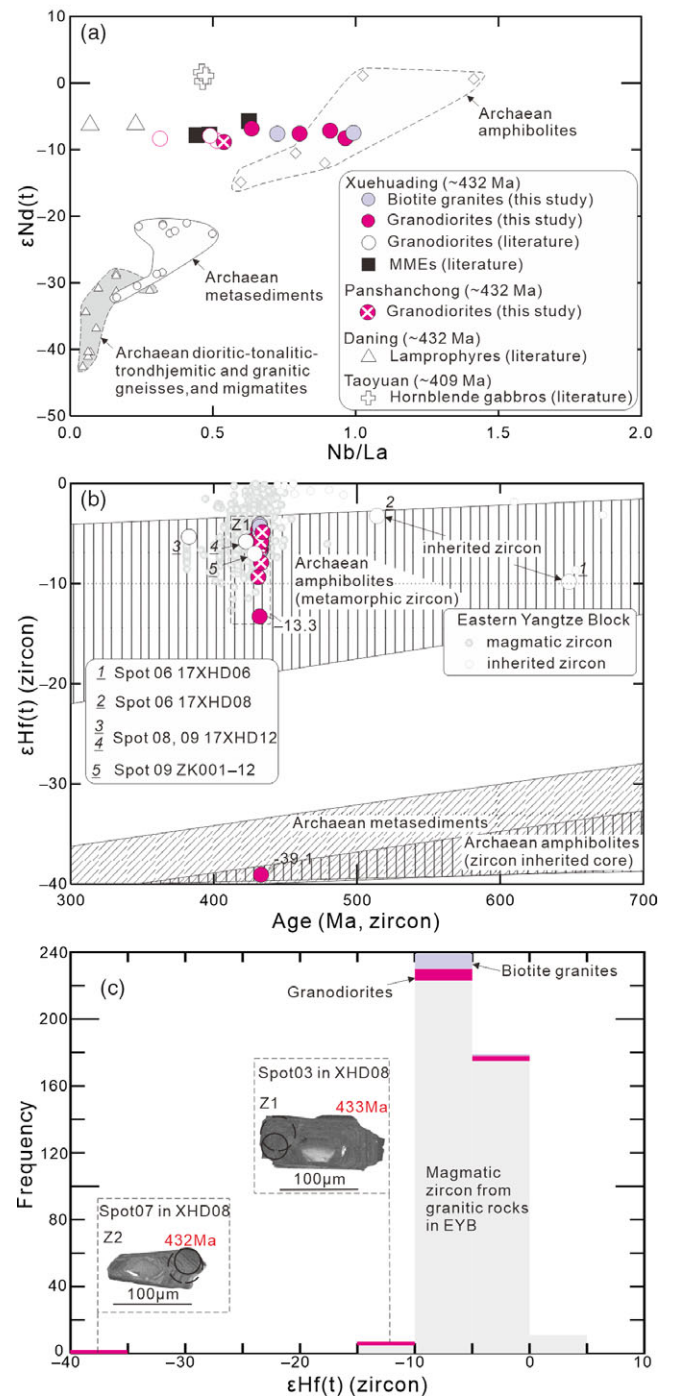


Fig. 8. (Colour online) Whole-rock initial Nd and zircon Hf isotope compositions for the studied granitic rocks. (a) $\epsilon\text{Nd}(t)$ values versus Nb/La ratios diagram. The data for Archaean amphibolites, metasediments and dioritic–tonalitic–trondhjemitic and granitic gneisses, and migmatites are from Gao *et al.* (1999) and Zhang *et al.* (2006). MMEs – mafic microgranular enclaves. (b) Zircon $\epsilon\text{Hf}(t)$ versus U–Pb age (Ma) diagram. (c) Magmatic zircon $\epsilon\text{Hf}(t)$ frequency distribution from middle Palaeozoic granitic rocks in the Eastern Yangtze Block. The data for the magmatic zircon $\epsilon\text{Hf}(t)$ are from Ou *et al.* (2019). The solid and dashed black circles on the zircon CL images indicate the locations of the U–Pb age and Hf isotope sites, respectively. The zircon Hf isotopic evolution field of the Kongling Archaean amphibolites (metamorphic and inherited core zircon) and the Archaean metasediments are from Zhang *et al.* (2006). Other data sources are as in Figure 6.

crust. At a deeper crustal level, garnet controls partitioning of HREEs and Y between the melt and solid phase during partial melting (Huang & He, 2010), and can substantially fractionate both the

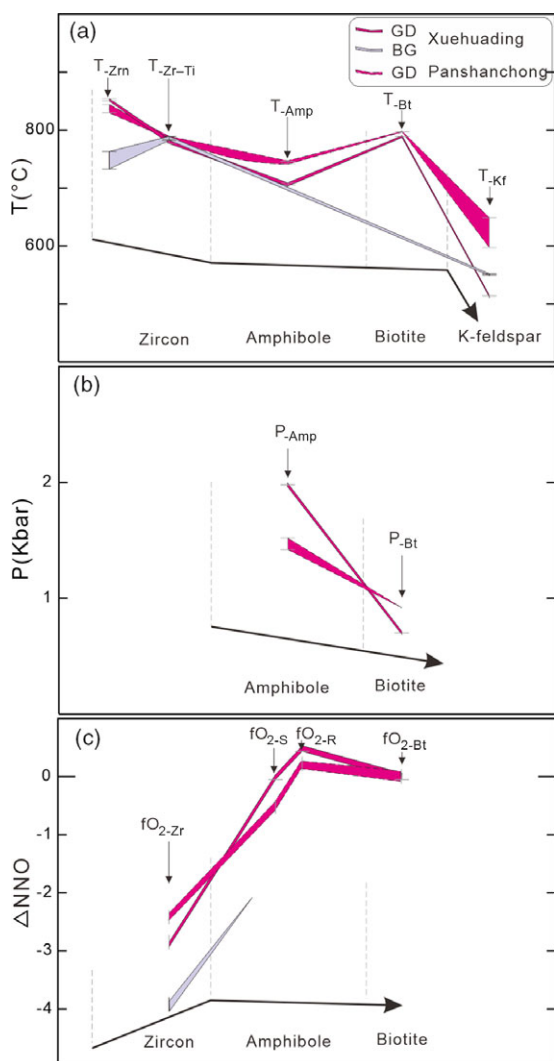


Fig. 9. (Colour online) Results of mineral crystallization conditions: (a) temperature, (b) pressure and (c) oxygen fugacity.

(La/Yb)_N and (Dy/Yb)_N of magmas (Blundy & Wood, 1994; Klein *et al.* 2000; Pertermann *et al.* 2004). However, the trace-element signature of the granodiorites does not suggest the presence of garnet in their crustal source (Fig. 10e, f). Moreover, the studied granitic rocks show similar whole-rock Nd and magmatic zircon Hf isotopic data to the Archaean amphiboles from the Kongling Complex, which represents the basement of the Yangtze Block (Gao *et al.* 1999; Zhang *et al.* 2006). Therefore, the studied granitic rocks were most probably generated by partial melting of amphibolites.

Figure 11b shows the results of the melting model, using REE data to account for primitive granodiorites by partial melting of amphibolites. The results of the modelling show that the primitive granodiorites could be reproduced by 20% batch melting (Fig. 11b; online Supplementary Material Table S8).

5.3.2. Genesis of the enclaves

Enclaves hosted by the granodiorites in XHD have fine-grained igneous textures (Fig. 2c, d), and a compositional gap with the contemporary mafic rocks in the Eastern Yangtze Block (Fig. 6), thus precluding the possibility of an origin from foreign xenoliths (e.g. country rocks) (e.g. Bacon, 1986; Mass *et al.* 1997; Xu *et al.* 2006)

and fractional crystallization. The opposite evolutionary trend in some elements or their ratios (e.g. CaO, Dy/Yb and Nb/Ta ratios versus SiO₂) (Fig. 6d) between the enclaves and their host granitic rocks cannot be explained by a mixing model (Karsli *et al.* 2007; Yang *et al.* 2007a,b).

None of models discussed above are applicable to the enclaves in this study. Instead, field observations and petrographic and geochemical data suggest that these enclaves were formed in a dominantly closed system; possible scenarios are discussed below.

The studied enclaves show trace-element compositions similar to their host rocks (Figs 6, 7), and therefore are unlikely to represent restites, which have a complementary composition to their host rocks (e.g. Chappell *et al.* 1987; Chappell & Wyborn, 2012). Crystal settling at the bottom of the magma chamber has been proposed to account for the formation of cognate cumulate enclaves that have mineral assemblages and geochemical and isotopic compositions similar to their host granites (Barbarin & Didier, 1992). Mafic minerals in enclaves are considered to be formed at an earlier stage of the same magma system and be similar to their host granitic rocks. However, the enclaves investigated in this study have small and less automorphic mineral grain sizes (Cheng *et al.* 2009) than the cumulate texture with a framework of touching subhedral to euhedral crystals described by Irvine (1982).

Previous work of Langmuir (1989) suggested that magma chamber margins are probable sites of solidification, where heat is lost and thermal and mechanical boundary layers may occur. The term ‘*in situ* crystallization’ was given in order to distinguish it from the concept of bottom crystallization (Campbell, 1978; Mcbirney & Noyes, 1979) or the autolith model (Tindle & Pearce, 1983; Barbarin & Didier, 1992; Schönerberger *et al.* 2006; Shellnutt *et al.* 2010). However, enclaves formed from this *in situ* model always show high mafic mineral concentrations, and some may be up to 50 modal per cent, owing to the continuous heat loss and crystallization (Langmuir, 1989). Considering this inconsistency, Donaire *et al.* (2005) suggested that the enclaves most probably form from their host granitic magma by kinetically induced accelerated crystallization of ferromagnesian (mafic) minerals related to rapid cooling when the magma is ascending in the feeding conduits. This interpretation would differ from *in situ* crystallization because there is no strict constraint on the number of mafic minerals that can be formed in the solidification zone, apart from the availability of elemental contents (Donaire *et al.* 2005). This rapid cooling model has a physicochemical basis in the theory of nucleation (Kirkpatrick, 1983) and the experiments of Naney & Swanson (1980), which suggested that mafic minerals (ino- and phyllosilicates) should nucleate more quickly than the framework silicates (e.g. feldspars and quartz) during the earliest crystallization of a silicate melt.

Accordingly, the enclaves in this study likely formed at the borders of ascending conduits during the granitic magma emplacement, where the mafic mineral crystallization was enhanced by rapid cooling (Naney & Swanson, 1980; Kirkpatrick, 1983). In this way, it is easy to explain the two different evolutionary trends of the enclaves and their host granitic rocks on the Harker diagrams (Fig. 6). For instance, the Dy/Yb, Nb/Ta ratios versus SiO₂ variations are the direct consequence of the amphibole concentration, owing to a partition coefficient of Kd(Dy)/Kd(Yb) > 1 (Tiepolo *et al.* 2001) and Kd(Nb)/Kd(Ta) > 1 (Sisson, 1994) in low-Mg amphibole. Similarly, the Cr–SiO₂ variations, deviating from the normal differentiation trend, would be caused by the rapid nucleation of amphibole (Kd(Cr) > 1 of amphibole in granitic magma;

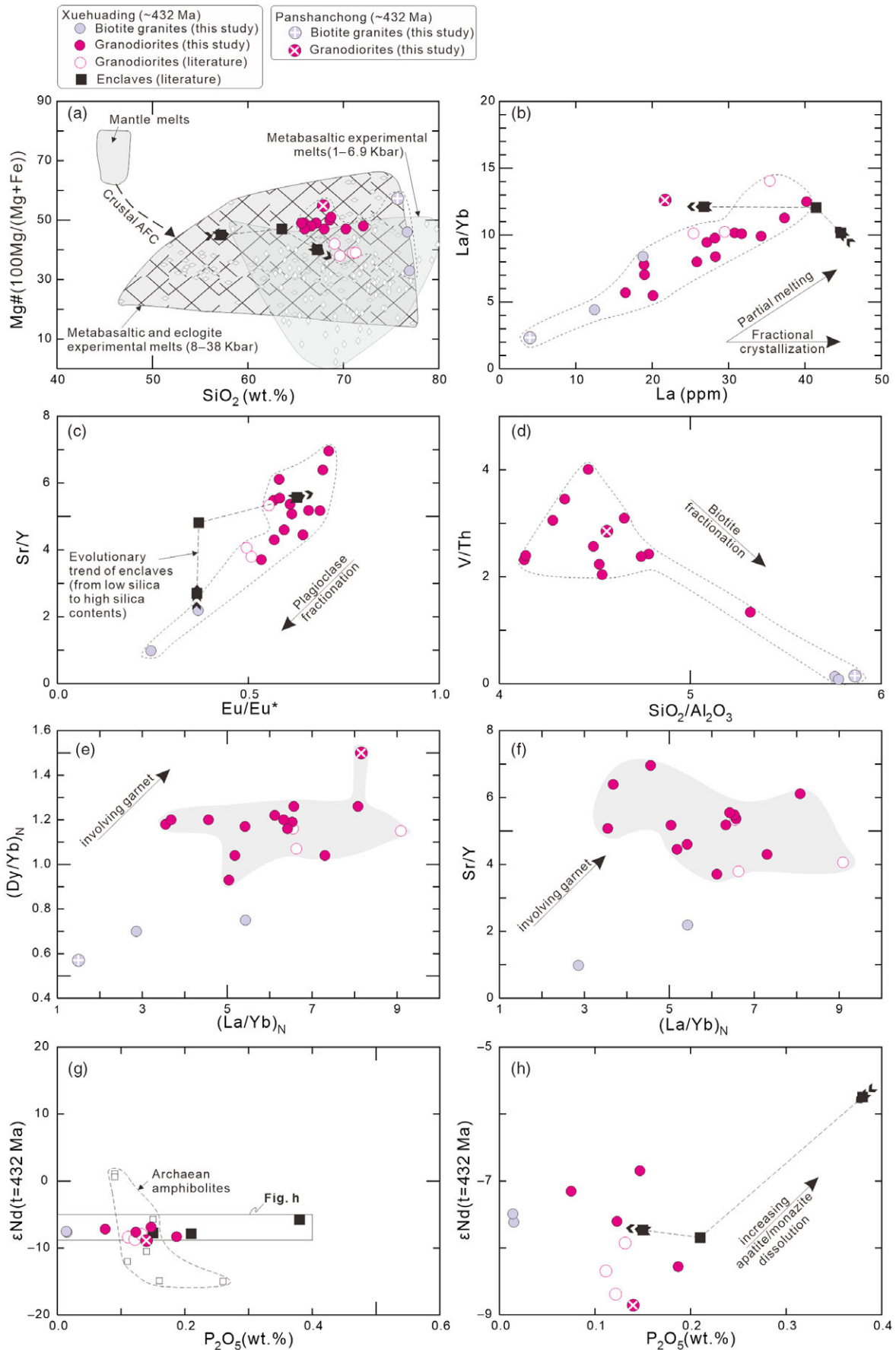


Fig. 10. (Colour online) (a) Diagram of Mg no. versus SiO₂ (wt %). Fields of metabasaltic experimental melts (1–6.9 kbar) (Beard & Lofgren, 1991) and metabasaltic and eclogite experimental melts (8–38 kbar) (Sen & Dunn, 1994; Rapp & Watson, 1995; Rapp *et al.* 2002; Skjerlie & Douce, 2002) are shown. Model curves of AFC process and mantle melts are after Wang *et al.* (2006). (b) La/Yb versus La (ppm) diagram, presenting a coherent partial melting trend for the studied granitic rocks. (c) Sr/Y versus Eu/Eu* and (d) V/Th versus SiO₂/Al₂O₃ diagram, displaying, respectively, the fractionation trends of plagioclase and biotite. (e) (Dy/Yb)_N and (f) Sr/Y versus (La/Yb)_N showing role of garnet in fractionating REEs to produce the composition of the studied granitic rocks during partial melting. (g) εNd(t = 432 Ma) values versus P₂O₅ (wt %) and (h) enlarged section, showing the influence of apatite/monazite dissolution (Zeng *et al.* 2005b). Other data sources are as Figure 6.

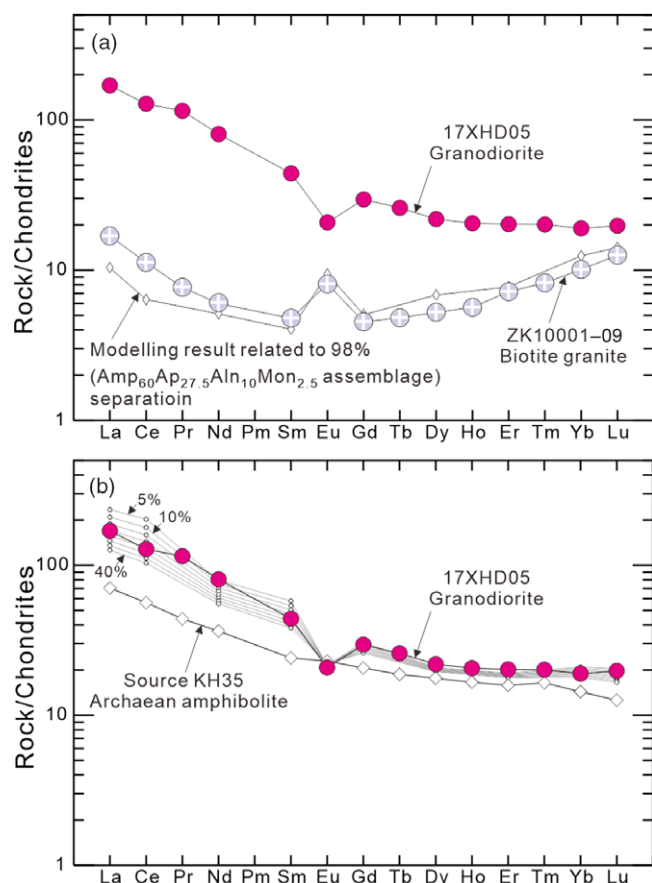


Fig. 11. (Colour online) REE modelling for the studied granitic rocks. (a) Modelling of formation of concave REE patterns through 98% fractionation ($\text{Amp}_{60}\text{Ap}_{27.5}\text{Aln}_{10}\text{Mon}_{2.5}$) from primitive granodiorites. Amp – amphibole; Ap – apatite; Aln – allanite; Mon – monazite. (b) Model curves of batch melting of Archaean amphibolite (KH35; Zhang *et al.* 2006) and primitive granodiorites (represented by 17XHD05). Symbols and data sources are as in Figure 6.

Sisson, 1994). Moreover, the different variation trends between the enclaves and their host granitic rocks in CaO and Sr versus SiO_2 diagrams suggest a compatible behaviour related to plagioclase precipitation, because both $\text{Kd}(\text{Ca})$ (Dudas *et al.* 1971; Nagasawa & Schnetzler, 1971) and $\text{Kd}(\text{Sr})$ (Philpotts & Schnetzler, 1970; Dudas *et al.* 1971; Nagasawa & Schnetzler, 1971; Ewart *et al.* 1973; Ewart & Griffin, 1994) of plagioclase in granitic magma are greater than one. It should be noted that the framework silicates (e.g. feldspars) also crystallized along with the mafic minerals (amphibole \pm biotite) in the rapid cooling zones proposed in this model (Donaire *et al.* 2005); however, crystallization of mafic minerals was enhanced.

5.c.3. The Nd–Hf isotopic heterogeneity

A common interpretation of isotopic variations in granitic plutons or batholiths is mantle-derived magma input (e.g. Yang *et al.* 2007a; Shaw & Flood, 2009; Tang *et al.* 2012). The premise of this interpretation is a homogeneous crustal source under the equilibrium melting process. However, a number of studies have advocated that much of the isotopic variation within the granitic rocks may be a near-source feature, primarily controlled by the source nature and melting conditions (Ayres & Harris, 1997; Davies & Tommasini, 2000; Zeng *et al.* 2005a,b; Tang *et al.* 2014; Huang *et al.* 2015; Hammerli *et al.* 2018). As discussed above,

the studied rocks were produced in a dominantly closed system, and their crustal source is similar to the Archaean amphibolites of the basement of the Yangtze Block. Therefore, the whole-rock Nd and zircon Hf isotopic heterogeneities in the studied rocks are probably inherited from their heterogeneous source or the result of disequilibrium melting processes.

The whole-rock Nd isotope signature of the studied rocks ranges from $\epsilon\text{Nd}(t)$ -8.86 to -5.75 (Fig. 8a; online Supplementary Material Table S4). Such variations (exceeding 3 epsilon units) in granitic plutons are commonly attributed to heterogeneities of their crustal sources (e.g. Huang *et al.* 2015). However, the coupling of anatexis reactions and dissolution of accessory phases plays a critical role in regulating the behaviour of the Sm–Nd isotope systems, and consequently generating Nd isotope disequilibrium (e.g. Zeng *et al.* 2005a,b). Apatite and monazite control the budget of Sm, Nd and P of these rocks (Ayres & Harris, 1997; Zeng *et al.* 2005b). In the $\epsilon\text{Nd}(t)$ versus P_2O_5 diagram (Fig. 10g, h), two groups can be observed: one is similar to Archaean amphibolites (assumed source rocks), and the other shows obviously higher $\epsilon\text{Nd}(t)$ and P_2O_5 values than the former. Therefore, enhanced dissolution of apatite or monazite into the melts is likely to have resulted in higher $\epsilon\text{Nd}(t)$ and P_2O_5 values during the disequilibrium melting processes (Zeng *et al.* 2005b).

The magmatic zircon $\epsilon\text{Hf}(t)$ values of the studied rocks range from -13.30 to -4.11 with a unimodal distribution (Z1), except for one outlier (Z2) of $c. -39.08$ (Fig. 8c). Zircons from the source (Archaean amphibolites) of the studied rocks have rim and core hafnium isotope ratios ($\epsilon\text{Hf}(t = 432 \text{ Ma})$) similar to the values of Z1 and Z2, respectively (Fig. 8b). Zircon is a ubiquitous Hf-enriched mineral in the continental crust (Tang *et al.* 2014). Therefore, in crustal sources, dissolution of zircons strongly controls the release of Hf into the melt. If Hf diffusivity of zircon in the crustal source is not rapid enough to reach equilibrium, the Hf isotope composition of the melt will be highly sensitive to the zircon dissolution rate during crustal anatexis (Flowerdew *et al.* 2006; Farina *et al.* 2014; Tang *et al.* 2014). Thus, the variation in $^{176}\text{Hf}/^{177}\text{Hf}$ ratios within the studied magmatic zircons from grain to grain indicates a variable zircon dissolution rate in the same magma source.

As discussed above, the Nd–Hf isotopic heterogeneity of the studied samples was not only controlled by their heterogeneous source but was also influenced by the disequilibrium melting process.

5.d. Implications

Our data suggest that the studied granitic rocks were mostly generated by partial melting of a metamafic source in the middle to lower crust and fractional crystallization without mantle-derived magma input (i.e. closed system). The related enclaves were formed at the margins of ascending conduits during the granitic magma emplacement. The detailed process is outlined in Figure 12 based on previous studies (e.g. Ou *et al.* 2019). In response to shortening and thickening of the crust in middle Palaeozoic time (pre-443 Ma) (Wan *et al.* 2010; Wang *et al.* 2011), a thickened lithospheric root was formed in the eastern SCB (Wang *et al.* 2013b; Peng *et al.* 2015). The subsequent tectonic collapse of the lithospheric mantle at the magmatic age peak ($c. 443\text{--}419 \text{ Ma}$; Wang *et al.* 2013b; Ou *et al.* 2019) would have caused the upwelling of the asthenosphere and raised the overall thermal budget of the lithosphere. Our previous study has shown that the thickened lithospheric root was delaminated into the

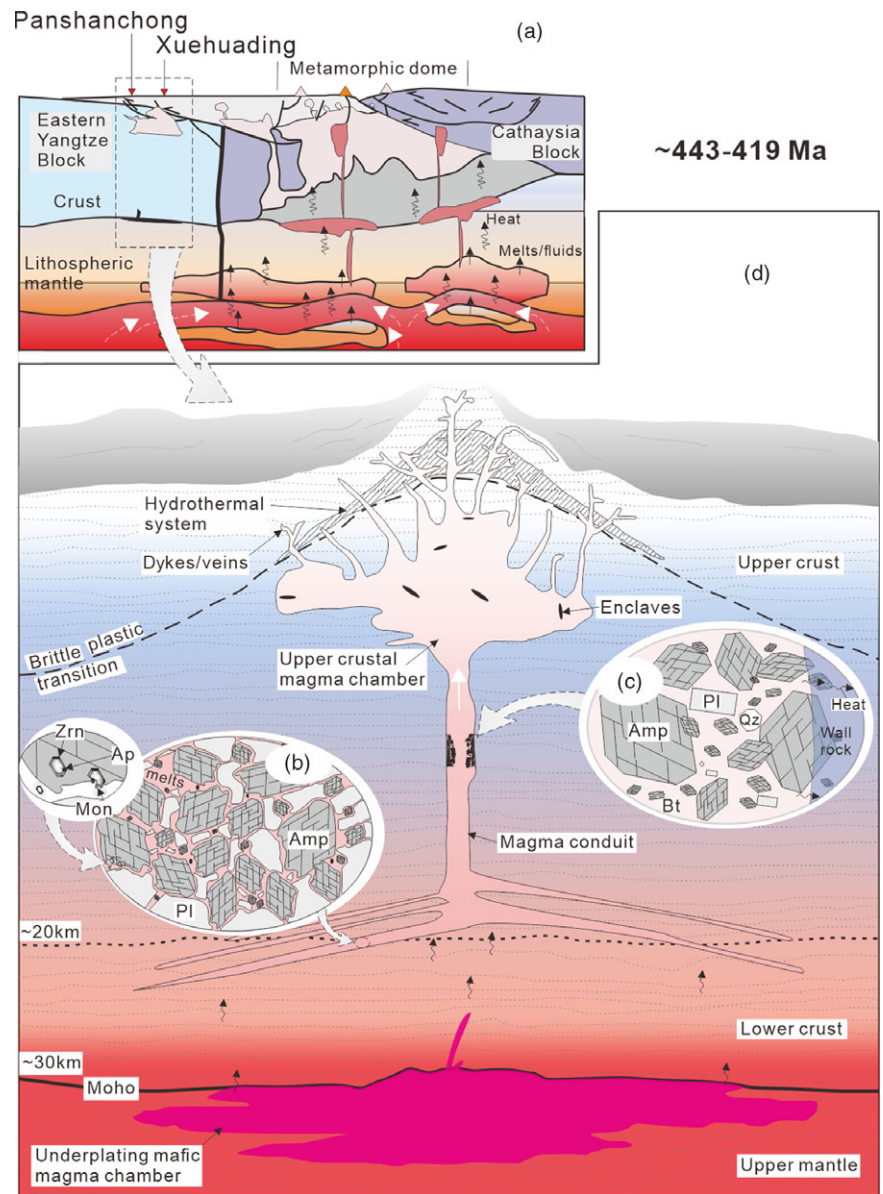


Fig. 12. (Colour online) Schematic depiction of the crustal source disequilibrium melting and rapid cooling model related to the studied granitic rocks after Donaire *et al.* (2005). (a) At 443–419 Ma, the repeated loss of the thickened lithospheric root and subsequent thermal upwelling in the SCB after Ou *et al.* (2019). (b) Early stages of melt generation from the disequilibrium melting of heterogeneous amphibolites in the middle–lower crust with variable rates of mineral dissolution/growth. (c) The incipient enclaves as totally or partially solidified bodies have formed at the borders of ascending conduits at a relatively early stage owing to the rapid cooling in these zones, and (d) later become incorporated into the primitive granodioritic magma during the magma emplacement (Donaire *et al.* 2005). (d) Deeper magma bodies emplaced in low-porosity crust may lose heat mainly by conduction, whereas at shallower levels hydrothermal fluid–melt interaction may be more significant (Spera & Bohron, 2004).

asthenospheric mantle as many independent parts below the metamorphic domes in the Cathaysia Block (Ou *et al.* 2019). This process is in agreement with a gravitational convective instability model with a slow foundering rate and piecemeal removal of the lithospheric root (Houseman & Molnar, 1997; Drew *et al.* 2009), instead of a rapid removal (Bird, 1979). During the repeated loss of the lithospheric root, continuous upwelling of the asthenosphere and emplacement of mafic magma at the base of the crust provided enough heat to the surrounding metamorphic domes (Fig. 12a). As a consequence, the Archaean amphibolites in the basement of the Yangtze Block underwent partial melting. The repeated thermal upwelling likely produced different batches of melts and resulted in the disequilibrium melting (Fig. 12b). Owing to such thermal disturbance, the simultaneous rate of mineral dissolution and isotopic equilibrium between the melt and residue was unable to be reached. In the relatively early stage, the enclaves formed at the borders of ascending conduits by rapid cooling in these zones (Fig. 12c), and were incorporated later into the granodioritic magma as partially solidified bodies during magma emplacement

(e.g. Donaire *et al.* 2005) (Fig. 12d). In this process, there is no thermal contrast between the enclaves–host rock, which is consistent with the lack of fine-grained chilled margins (Fig. 2c, d) in the studied enclaves. Moreover, there are some feldspar crystals that cross the boundaries into the enclaves (Fig. 2c, d), showing evidence of local, second-order mingling processes between the enclaves and host rocks (Fig. 12d). Accompanying the formation of the enclaves and the granodiorites, the biotite granites were generated through fractional crystallization from the granodiorite magma. One example of a biotite granite with a concave REE pattern probably resulted from a greater separation of accessory minerals and/or influence of hydrothermal fluid–melt interaction (Fig. 12d).

The recognition of rapid cooling in the formation of enclaves has a great significance in understanding the formation of the massive felsic batholith in the granitic province of the SCB, where mafic rocks represent only a minor component. This process has been verified by a series of experiments (Naney & Swanson, 1980; Kirkpatrick, 1983) and the exposure of magma conduits with the aggregation of fine-grained mafic minerals (Donaire *et al.* 2005). Some previous studies

continuously tried to emphasize the role of mafic magma in the petrogenesis of enclaves and their host rocks through magma-mixing processes (e.g. Karsli *et al.* 2007; Yang *et al.* 2007b; Zhang *et al.* 2016). However, the low ratio of mafic and granitic rocks in the exposed area and the lack of disequilibrium features of the minerals (e.g. core-rim textures) in the studied rocks are inconsistent with the magma-mixing process. In addition, the magma related to the studied granitic rocks experienced a normal evolutionary trend without abnormal perturbation of physicochemical conditions, thereby ruling out the magma-mixing process. The combination of Nd–Hf isotopic data with the mineral composition, whole-rock major and trace elements, and the different evolutionary trends between the enclaves and their host rocks provides robust evidence to identify the rapid cooling process and to determine their sources were without any direct mantle material contribution in the Eastern Yangtze Block. Moreover, the rapid cooling model could be applied to other massive felsic batholiths with similar microgranular enclaves/host rock relationships, especially where distinctive evidence (isotopic, mineralogical and textural aspects) for magma mixing is absent.

6. Conclusions

- (1) LA-ICP-MS zircon U–Pb dating shows that the host rocks (granodiorites and biotite granites) in the Xuehuading–Panshanhong area of the Eastern Yangtze Block were generated during middle Palaeozoic time (c. 432 Ma).
- (2) Enclaves (previous data and our investigation) and host rocks in the studied area have similar mineral assemblages, trace elements and isotopic compositions.
- (3) The granodiorites were most likely generated by disequilibrium partial melting of the Archaean heterogeneous amphibolites of the basement of Yangtze Block in the middle to lower crust. The biotite granites were the product of granodioritic magma through fractional crystallization.
- (4) The enclaves would have formed at the borders of ascending conduits during the granitic magma emplacement, where the mafic mineral crystallization was enhanced by rapid cooling compared to normal crystallization.
- (5) The piecemeal removal of the lithospheric root in middle Palaeozoic time provided repeated thermal disturbance to the crustal source of the Eastern Yangtze Block, west of the metamorphic domes in the Cathaysia Block, without direct mantle magma contribution to the granites.

Acknowledgements. We would like to thank Executive Editor Kathryn Goodenough and three anonymous reviewers for their constructive and helpful reviews. Presented data are available by request from the corresponding authors. Wen-Zhou Xiao, Ri-Jun Du, Ye Liu, Shuang-Lian Li, Chao-Yun Liu, Jun-Wei Xu, Meng-Zhao Li, Chang-Ming Xing, Hong-Xia Yu, Lan-Fang Xie, Yong-Hai Yuan, Jia-Cai Li and Liang Li are thanked for their assistance with field and laboratory work. Qi-Wei Li and Zong-Yong Yang are thanked for their many discussions about the basement of the Yangtze Block, concave REE patterns and so on. Financial support for this research was provided by the National Key R & D Programme of China (No. 2017YFC0602402), the National Natural Science Foundation of China (No. 41802057), the Provincial Natural Science Foundation of Hunan (No. 2019JJ50831), the China Postdoctoral Science Foundation (No. 2017M622597), the Funded by Open Research Fund Programme of the Key Laboratory of Metallogenic Prediction of Nonferrous Metals and Geological Environment Monitoring (Central South University), Ministry of Education (No. 2018YJSJ07), the research grant from the State Key Laboratory of Isotope Geochemistry, Guangzhou Institute of Geochemistry, Chinese Academy of Sciences (SKLabiG–KF–18–05), and the National Science and Technology Major Project “Study of Proterozoic tectonic-lithofacies palaeogeography in Sichuan

Basin” (No. 2017ZX05008005009). B.B.C. is thankful to Cariparo and MIUR (Ministero dell’ Istruzione, dell’Università e della Ricerca) for the award of post-doctoral grants (Makearth and PNRA18_00103).

Supplementary material. To view supplementary material for this article, please visit <https://doi.org/10.1017/S0016756820001144>.

References

- Al’meev RR, Ariskin AA, Ozerov AY and Kononkova NN (2002) Problems of the stoichiometry and thermobarometry of magmatic amphiboles: an example of hornblende from the andesites of Bezymianny volcano, eastern Kamchatka. *Geochemistry International* **40**, 723–38.
- Alves A, Janasi VA, Simonetti A and Heaman L (2009) Microgranitic enclaves as products of self-mixing events: a study of open-system processes in the Mauá Granite, São Paulo, Brazil, based on in situ isotopic and trace elements in plagioclase. *Journal of Petrology* **50**, 2221–47.
- Andersen T (2002) Correction of common lead in U–Pb analyses that do not report ²⁰⁴Pb. *Chemical Geology* **192**, 59–79.
- Ayres M and Harris N (1997) REE fractionation and Nd-isotope disequilibrium during crustal anatexis: constraints from Himalayan leucogranites. *Chemical Geology* **139**, 249–69.
- Bacon CR (1986) Magmatic inclusions in silicic and intermediate rocks. *Journal of Geophysical Research: Solid Earth* **91**, 6091–112.
- Barbarin B (2005) Mafic magmatic enclaves and mafic rocks associated with some granitoids of the central Sierra Nevada batholith, California: nature, origin, and relations with the hosts. *Lithos* **80**, 155–77.
- Barbarin B and Didier J (1992) Genesis and evolution of mafic microgranular enclaves through various types of interaction between coexisting felsic and mafic magmas. *Transactions of the Royal Society of Edinburgh: Earth Sciences* **83**, 145–53.
- Bea F (2010) Crystallization dynamics of granite magma chambers in the absence of regional stress: multiphysics modeling with natural examples. *Journal of Petrology* **51**, 1541–69.
- Bea F, Pereira MG and Stroh A (1994) Mineral/leucosome trace-element partitioning in a peraluminous migmatite (a laser ablation-ICP-MS study). *Chemical Geology* **117**, 291–312.
- Beard JS and Lofgren GE (1991) Dehydration melting and water-saturated melting of basaltic and andesitic greenstones and amphibolites at 1, 3, and 6.9 kb. *Journal of Petrology* **32**, 465–501.
- Belousova EA, Griffin WL, O’Reilly SY and Fisher NI (2002) Igneous zircon: trace element composition as an indicator of source rock type. *Contributions to Mineralogy and Petrology* **143**, 602–22.
- Bird P (1979) Continental delamination and the Colorado Plateau. *Journal of Geophysical Research: Solid Earth* **84**, 7561–71.
- Blundy J and Wood B (1994) Prediction of crystal–melt partition coefficients from elastic moduli. *Nature* **372**, 452–4.
- Browne BL, Eichelberger JC, Patino LC, Vogel TA, Dehn J, Uto K and Hoshizumi H (2006) Generation of porphyritic and equigranular mafic enclaves during magma recharge events at Unzen Volcano, Japan. *Journal of Petrology* **47**, 301–28.
- Campbell IH (1978) Some problems with the cumulus theory. *Lithos* **11**, 311–23.
- Carvalho BB, Sawyer EW and Janasi VA (2017) Enhancing maficity of granitic magma during anatexis: entrainment of infertile mafic lithologies. *Journal of Petrology* **58**, 1333–62.
- Chappell BW (1996) Magma mixing and the production of compositional variation within granite suites: evidence from the granites of Southeastern Australia. *Journal of Petrology* **37**, 449–70.
- Chappell BW and Stephens WE (1988) Origin of infracrustal (I-type) granite magmas. *Transactions of the Royal Society of Edinburgh: Earth Sciences* **79**, 71–86.
- Chappell BW and White AJR (1992) I- and S-type granites in the Lachlan Fold Belt. *Transactions of the Royal Society of Edinburgh: Earth Sciences* **83**, 1–26.
- Chappell BW, White AJR and Wyborn D (1987) The importance of residual source material (restite) in granite petrogenesis. *Journal of Petrology* **28**, 1111–38.

- Chappell BW and Wyborn D** (2012) Origin of enclaves in S-type granites of the Lachlan Fold Belt. *Lithos* **154**, 235–47.
- Charvet J, Shu LS, Faure M, Choulet F, Wang B, Lu HF and Breton NL** (2010) Structural development of the lower Paleozoic belt of South China: genesis of an intracontinental orogen. *Journal of Asian Earth Science* **39**, 309–30.
- Chen B, Chen ZC and Jahn BM** (2009) Origin of mafic enclaves from the Taihang Mesozoic Orogen, North China Craton. *Lithos* **110**, 343–58.
- Chen JF and Jahn BM** (1998) Crustal evolution of southeastern China: Nd and Sr isotopic evidence. *Tectonophysics* **284**, 101–33.
- Cheng SB, Fu JM, Xu DM, Ma LY, Pang YC and Cao L** (2009) Geochemical characteristics and petrogenesis of Xuehuading granitic batholith and its enclaves, South China. *Geotectonica et Metallogenia* **33**, 588–97 (in Chinese with English abstract).
- Clarke DB and Carruzzo S** (2007) Assimilation of country-rock ilmenite and rutile in the South Mountain Batholith, Nova Scotia, Canada. *The Canadian Mineralogist* **45**, 31–42.
- Davies GR and Tommasini S** (2000) Isotopic disequilibrium during rapid crustal anatexis: implications for petrogenetic studies of magmatic processes. *Chemical Geology* **162**, 169–91.
- Didier J** (1973) *Granites and their Enclaves: The Bearing of Enclaves on the Origin of Granites*. Developments in Petrology, Vol. 3. Amsterdam: Elsevier.
- Domenick MA, Kistler RW, Dodge FCW and Tatsumoto M** (1983) Nd and Sr isotopic study of crustal and mantle inclusions from the Sierra Nevada and implications for batholith petrogenesis. *Geological Society of America Bulletin* **94**, 713–19.
- Donaire T, Pascual E, Pin C and Douthou JL** (2005) Microgranular enclaves as evidence of rapid cooling in granitoid rocks: the case of the Los Pedroches granodiorite, Iberian Massif, Spain. *Contributions to Mineralogy and Petrology* **149**, 247–65.
- Dostal J, Kontak DJ, Gerel O, Shellnutt JG and Fayek M** (2015) Cretaceous ongonites (topaz-bearing albite-rich microleucogranites) from Ongon Khaikhan, Central Mongolia: products of extreme magmatic fractionation and pervasive metasomatic fluid: rock interaction. *Lithos* **236–237**, 173–89.
- Drew ST, Ducea MN and Schoenbohm LM** (2009) Mafic volcanism on the Puna Plateau, NW Argentina: implications for lithospheric composition and evolution with an emphasis on lithospheric foundering. *Lithosphere* **1**, 305–18.
- Dudas MJ, Schmitt RA and Harward ME** (1971) Trace element partitioning between volcanic plagioclase and dacitic pyroclastic matrix. *Earth and Planetary Science Letters* **11**, 440–6.
- Ewart A, Bryan WB and Gill JB** (1973) Mineralogy and geochemistry of the younger volcanic islands of Tonga, S.W. Pacific. *Journal of Petrology* **14**, 429–65.
- Ewart A and Griffin WL** (1994) Application of proton-microprobe data to trace-element partitioning in volcanic rocks. *Chemical Geology* **117**, 251–84.
- Farina F, Stevens G, Gerdes A and Frei D** (2014) Small-scale Hf isotopic variability in the Peninsula pluton (South Africa): the processes that control inheritance of source $^{176}\text{Hf}/^{177}\text{Hf}$ diversity in S-type granites. *Contributions to Mineralogy and Petrology* **168**, 1–18.
- Farner MJ, Lee CTA and Putirka KD** (2014) Mafic–felsic magma mixing limited by reactive processes: a case study of biotite-rich rinds on mafic enclaves. *Earth and Planetary Science Letters* **393**, 49–59.
- Faure M, Shu LS, Wang B, Charvet J, Choulet F and Monie P** (2009) Intracontinental subduction: a possible mechanism for the early Palaeozoic orogen of SE China. *Terra Nova* **21**, 360–8.
- Flowerdew MJ, Millar IL, Vaughan APM, Horstwood MSA and Fanning CM** (2006) The source of granitic gneisses and migmatites in the Antarctic Peninsula: a combined U–Pb SHRIMP and laser ablation Hf isotope study of complex zircons. *Contributions to Mineralogy and Petrology* **151**, 751–68.
- Foster MD** (1960) *Interpretation of the Composition of Trioctahedral Micas*. Geological Survey Professional Paper 354–B. Washington: United States Government Printing Office.
- Fu JM, Ma CQ, Xie CF, Zhang YM and Peng SB** (2004) SHRIMP U–Pb zircon dating of the Jiuyishan composite granite in Hunan and its geological significance. *Geotectonica et Metallogenia* **28**, 370–8 (in Chinese with English abstract).
- Gao S, Ling WL, Qiu Y, Lian Z, Hartmann G and Simon K** (1999) Contrasting geochemical and Sm–Nd isotopic compositions of Archean metasediments from the Kongling high-grade terrain of the Yangtze craton: evidence for cratonic evolution and redistribution of REE during crustal anatexis. *Geochimica et Cosmochimica Acta* **63**, 2071–88.
- Geng JZ, Li HK, Zhang J, Zhou HY and Li HM** (2011) Zircon Hf isotope analysis by means of LA-MC-ICP-MS. *Geological Bulletin of China* **30**, 1508–13 (in Chinese with English abstract).
- Hammerli J, Kemp AIS, Shimura T, Vervoort JD and Dunkley DJ** (2018) Generation of I-type granitic rocks by melting of heterogeneous lower crust. *Geology* **46**, 907–10.
- Hammouda T, Pichavant M and Chaussidon M** (1996) Isotopic equilibration during partial melting: an experimental test of the behaviour of Sr. *Earth and Planetary Science Letters* **144**, 109–21.
- Hawkesworth CJ, Blake S, Evans P, Hughes R, Macdonald R, Thomas E, Turner SP and Zellmer G** (2000) Time scales of crystal fractionation in magma chambers – integrating physical, isotopic and geochemical perspectives. *Journal of Petrology* **41**, 991–1006.
- Hawkesworth CJ, George R, Turner S and Zellmer G** (2004) Time scales of magmatic processes. *Earth and Planetary Science Letters* **218**, 1–16.
- Hogan JP and Sinha AK** (1991) The effect of accessory minerals on the redistribution of lead isotopes during crustal anatexis: a model. *Geochimica et Cosmochimica Acta* **55**, 335–48.
- Holden P, Halliday AN and Stephens WE** (1987) Neodymium and strontium isotope content of microdiorite enclaves points to mantle input to granitoid production. *Nature* **330**, 53–6.
- Hoskin PWO** (2005) Trace-element composition of hydrothermal zircon and the alteration of Hadean zircon from the Jack Hills, Australia. *Geochimica et Cosmochimica Acta* **69**, 637–48.
- Houseman GA and Molnar P** (1997) Gravitational (Rayleigh–Taylor) instability of a layer with non-linear viscosity and convective thinning of continental lithosphere. *Geophysical Journal International* **128**, 125–50.
- Huang F and He YS** (2010) Partial melting of the dry mafic continental crust: implications for petrogenesis of C-type adakites. *Chinese Science Bulletin* **55**, 2428–39.
- Huang HQ, Li XH, Li ZX and Li WX** (2015) Formation of the Jurassic South China Large Granitic Province: insights from the genesis of the Jiufeng pluton. *Chemical Geology* **401**, 43–58.
- Huang XL, Xu YG, Lo CH, Wang RC and Lin CY** (2007) Exsolution lamellae in a clinopyroxene megacryst aggregate from Cenozoic basalt, Leizhou Peninsula, South China: petrography and chemical evolution. *Contributions to Mineralogy and Petrology* **154**, 691–705.
- Irvine TN** (1982) Terminology for layered intrusions. *Journal of Petrology* **23**, 127–62.
- Jackson SE, Pearson NJ, Griffin WL and Belousova EA** (2004) The application of laser ablation-inductively coupled plasma-mass spectrometry to in situ U–Pb zircon geochronology. *Chemical Geology* **211**, 47–69.
- Jia XH, Wang XD and Yang WQ** (2017) Petrogenesis and geodynamic implications of the early Paleozoic potassic and ultrapotassic rocks in the South China Block. *Journal of Asian Earth Science* **135**, 80–94.
- Karsli O, Chen B, Aydin F and Şen C** (2007) Geochemical and Sr–Nd–Pb isotopic compositions of the Eocene Dölek and Sarıçiçek plutons, Eastern Turkey: implications for magma interaction in the genesis of high-K calc-alkaline granitoids in a post-collision extensional setting. *Lithos*, **98**, 67–96.
- Kirkpatrick RJ** (1983) Theory of nucleation in silicate melts. *American Mineralogist* **68**, 66–77.
- Klein M, Stosch HG, Seck H and Shimizu N** (2000) Experimental partitioning of high field strength and rare earth elements between clinopyroxene and garnet in andesitic to tonalitic systems. *Geochimica et Cosmochimica Acta* **64**, 99–115.
- Knesel KM and Davidson JP** (1996) Isotopic disequilibrium during melting of granite and implications for crustal contamination of magmas. *Geology* **24**, 243–6.
- Langmuir CH** (1989) Geochemical consequences of in situ crystallization. *Nature* **340**, 199–205.
- Leake B, Woolley A, Arps C, Birch W, Gilbert M, Grice J, Hawthorn F, Kato A, Kisch H and Krivovichev V** (1997) Nomenclature of amphiboles: report of the subcommittee on amphiboles of the International Mineralogical Association, Commission on New Minerals and Mineral Names. *American Mineralogist* **82**, 1019–37.

- Li XH, Li WX, Li ZX and Liu Y (2008) 850–790 Ma bimodal volcanic and intrusive rocks in northern Zhejiang, South China: a major episode of continental rift magmatism during the breakup of Rodinia. *Lithos* **102**, 341–57.
- Li XH, Li ZX, Li WX, Liu Y, Yuan C, Wei GJ and Qi CS (2007) U–Pb zircon, geochemical and Sr–Nd–Hf isotopic constraints on age and origin of Jurassic I- and A-type granites from central Guangdong, SE China: a major igneous event in response to foundering of a subducted flat-slab? *Lithos* **96**, 186–204.
- Li XH, Li WX, Li ZX, Lo CH, Wang J, Ye MF and Yang YH (2009) Amalgamation between the Yangtze and Cathaysia Blocks in South China: constraints from SHRIMP U–Pb zircon ages, geochemistry and Nd–Hf isotopes of the Shuangxiwu volcanic rocks. *Precambrian Research* **174**, 117–28.
- Li ZX, Li XH, Wartho JA, Clark C, Li WX, Zhang CL and Bao CM (2010) Magmatic and metamorphic events during the early Paleozoic Wuyi–Yunkai orogeny, southeastern South China: new age constraints and pressure–temperature conditions. *Geological Society of America Bulletin* **122**, 772–93.
- Li XH, Li ZX, Wingate MT, Chung SL, Liu Y, Lin GC and Li WX (2006) Geochemistry of the 755 Ma Mundine Well dyke swarm, northwestern Australia: part of a Neoproterozoic mantle superplume beneath Rodinia? *Precambrian Research* **146**, 1–15.
- Li XH, Liu DY, Sun M, Li WX, Liang XR and Liu Y (2004) Precise Sm–Nd and U–Pb isotopic dating of the supergiant Shizhuyuan polymetallic deposit and its host granite, SE China. *Geological Magazine* **141**, 225–31.
- Liu YS, Hu ZC, Zong KQ, Gao CG, Gao S, Xu J and Chen HH (2010) Reappraisal and refinement of zircon U–Pb isotope and trace element analyses by LA-ICP-MS. *Science Bulletin* **55**, 1535–46.
- Liu Y, Lai JQ, Xiao WZ, Jeffrey D, Du RJ, Li SL, Liu CY, Wen CH and Yu XH (2019) Petrogenesis and mineralization of two-stage A-type granites in Jiuyishan, South China: constraints from whole-rock geochemistry, mineral composition and zircon U–Pb–Hf isotopes. *Acta Geologica Sinica (English edition)* **93**, 874–900.
- Liu CQ and Zhang H (2005) The lanthanide tetrad effect in apatite from the Altay no. 3 pegmatite, Xingjiang, China: an intrinsic feature of the pegmatite magma. *Chemical Geology* **214**, 61–77.
- Ludwig KR (2003) *User's Manual for Isoplot 3.00: A Geochronological Toolkit for Microsoft Excel*. Berkeley Geochronology Center, Special Publication no. 4.
- Ma CQ, Yang KG, Tang ZH and Li ZT (1994) *Magma-Dynamics Granitoids: Theory, Methods and a Case Study of the Eastern Hubei Granitoids*. Wuhan: China University of Geosciences Press, pp. 169–73 (in Chinese).
- Maruël P, Cuney M and Turpin L (1990) Magmatic and hydrothermal R.E.E. fractionation in the Xihuashan granites (SE China). *Contributions to Mineralogy and Petrology* **104**, 668–80.
- Mass R, Nicholls IA and Legg C (1997) Igneous and metamorphic enclaves in the S-type Deddick granodiorite, Lachlan Fold Belt, SE Australia: petrographic, geochemical and Nd–Sr isotopic evidence for crustal melting and magma mixing. *Journal of Petrology* **38**, 815–41.
- McBirney AR and Noyes RM (1979) Crystallization and layering of the Skaergaard intrusion. *Journal of Petrology* **20**, 487–554.
- McKay G, Le L, Wagstaff J and Crozaz G (1994) Experimental partitioning of rare earth elements and strontium: constraints on petrogenesis and redox conditions during crystallization of Antarctic angrite Lewis Cliff 86010. *Geochimica et Cosmochimica Acta* **58**, 2911–19.
- Miller CF (1985) Are strongly peraluminous magmas derived from pelitic sedimentary sources? *Journal of Geology* **93**, 673–89.
- Miller CF, Stoddard EF, Bradfish LJ and Dollase WA (1981) Composition of plutonic muscovite: genetic implications. *The Canadian Mineralogist* **19**, 25–34.
- Morel M, Nebel O, Nebel-Jacobsen Y, Miller J and Vroon P (2008) Hafnium isotope characterization of the GJ-1 zircon reference material by solution and laser-ablation MC-ICPMS. *Chemical Geology* **255**, 231–5.
- Nacht H, Ibhi A, Abia EH and Ohoud MB (2005) Discrimination between primary magmatic biotites, reequilibrated biotites and neoformed biotites. *Comptes Rendus Geosciences* **337**, 1415–20.
- Nagasawa H and Schnetzler CC (1971) Partitioning of rare earth, alkali and alkaline earth elements between phenocrysts and acidic igneous magma. *Geochimica et Cosmochimica Acta* **35**, 953–68.
- Naney MT and Swanson SE (1980) The effect of Fe and Mg on crystallization in granitic systems. *American Mineralogist* **65**, 639–53.
- Niu YL, Zhao ZD, Zhu DC and Mo XX (2013) Continental collision zones are primary sites for net continental crust growth – a testable hypothesis. *Earth-Science Reviews* **127**, 96–110.
- Ou Q, Lai JQ, Carvalho BB, Zi F, Kong H, Li B and Jiang ZQ (2019) Different response to middle–Palaeozoic magmatism during intracontinental orogenic processes: evidence from southeastern South China Block. *International Geology Review* **61**, 1504–21.
- Peate DW, Barker AK, Riisshuus MS and Andreassen R (2008) Temporal variations in crustal assimilation of magma suites in the East Greenland flood basalt province: tracking the evolution of magmatic plumbing systems. *Lithos* **102**, 179–97.
- Peccerillo A and Taylor SR (1976) Geochemistry of Eocene calc-alkaline volcanic rocks from the Kastamonu area, northern Turkey. *Contributions to Mineralogy and Petrology* **58**, 63–81.
- Peng TP, Fan WM, Zhao GW, Peng BX, Xia XP and Mao YS (2015) Petrogenesis of the early Paleozoic strongly peraluminous granites in the western South China Block and its tectonic implications. *Journal of Asian Earth Science* **98**, 399–420.
- Pertermann M, Hirschmann M, Hametner K, Günther D and Schmidt M (2004) Experimental determination of trace element partitioning between garnet and silica-rich liquid during anhydrous partial melting of MORB-like eclogite. *Geochemistry, Geophysics, Geosystems* **5**, 1–23.
- Philpotts JA and Schnetzler CC (1970) Phenocryst–matrix partition coefficients for K, Rb, Sr and Ba, with applications to anorthosite and basalt genesis. *Geochimica et Cosmochimica Acta* **34**, 307–22.
- Preston RJ, Bell BR and Rogers G (1998) The Loch Scridain xenolithic sill complex, Isle of Mull, Scotland: fractional crystallization, assimilation, magma-mixing and crustal anatexis in subvolcanic conduits. *Journal of Petrology* **39**, 519–50.
- Qiu YM, Gao S, McNaughton NJ, Groves DI and Ling WL (2000) First evidence of >3.2 Ga continental crust in the Yangtze craton of south China and its implications for Archean crustal evolution and Phanerozoic tectonics. *Geology* **28**, 11–14.
- Rapp RP and Watson EB (1995) Dehydration melting of metabasalt at 8–32 kbar: implications for continental growth and crust–mantle recycling. *Journal of Petrology* **36**, 891–931.
- Rapp RP, Xiao L and Shimizu N (2002) Experimental constraints on the origin of potassium-rich adakites in eastern China. *Acta Petrologica Sinica* **18**, 293–302.
- Rong W, Zhang SB and Zheng YF (2017) Back-reaction of peritectic garnet as an explanation for the origin of mafic enclaves in S-type granite from the Jiuling batholith in South China. *Journal of Petrology* **58**, 569–98.
- Schönenberger J, Marks M, Wagner T and Markl G (2006) Fluid–rock interaction in autoliths of apatitic nepheline syenites in the Ilimaussaq intrusion, South Greenland. *Lithos* **91**, 331–51.
- Sen C and Dunn T (1994) Dehydration melting of a basaltic composition amphibolite at 1.5 and 2.0 GPa: implications for the origin of adakites. *Contributions to Mineralogy and Petrology* **117**, 394–409.
- Shaw SE and Flood RH (2009) Zircon Hf isotopic evidence for mixing of crustal and silicic mantle-derived magmas in a zoned granite pluton, Eastern Australia. *Journal of Petrology* **50**, 147–68.
- Shellnutt JG, Jahn BM and Dostal J (2010) Elemental and Sr–Nd isotope geochemistry of microgranular enclaves from peralkaline A-type granitic plutons of the Emeishan large igneous province, SW China. *Lithos* **119**, 34–46.
- Sheth HC (2007) 'Large Igneous Provinces (LIPs)': definition, recommended terminology, and a hierarchical classification. *Earth-Science Reviews* **85**, 117–24.
- Sisson TW (1994) Hornblende–melt trace-element partitioning measured by ion microprobe. *Chemical Geology* **117**, 331–44.
- Skjerlie KP and Douce AEP (2002) The fluid-absent partial melting of a zoisite-bearing quartz eclogite from 1.0 to 3.2 GPa; implications for melting in

- thickened continental crust and for subduction-zone processes. *Journal of Petrology* **43**, 291–314.
- Sláma J, Košler J, Condon DJ, Crowley JL, Gerdes A, Hanchar JM, Horstwood MSA, Morris GA, Nasdala L, Norberg N, Schaltegger U, Schoene B, Tubrett MN and Whitehouse MJ** (2008) Plešovice zircon – a new natural reference material for U–Pb and Hf isotopic microanalysis. *Chemical Geology* **249**, 1–35.
- Spera FJ and Bohron WA** (2004) Open-system magma chamber evolution: an energy-constrained geochemical model incorporating the effects of concurrent eruption, recharge, variable assimilation and fractional crystallization (EC-E'RA γ FC). *Journal of Petrology* **45**, 2459–80.
- Sun SS and McDonough W** (1989) Chemical and isotopic systematics of oceanic basalts: implications for mantle composition and processes. In *Magmatism in the Ocean Basins* (eds AD Saunders and MJ Norry), pp. 313–45. Geological Society of London, Special Publication no. 42.
- Sun JF, Yang JH, Wu FY, Li XH, Yang YH, Xie LW and Wilde SA** (2010) Magma mixing controlling the origin of the Early Cretaceous Fangshan granitic pluton, North China Craton: *in situ* U–Pb age and Sr-, Nd-, Hf- and O-isotope evidence. *Lithos* **120**, 421–38.
- Tang M, Wang XL, Shu XJ, Wang D, Yang T and Gopon P** (2014) Hafnium isotopic heterogeneity in zircons from granitic rocks: geochemical evaluation and modeling of “zircon effect” in crustal anatexis. *Earth and Planetary Science Letters* **389**, 188–99.
- Tang GJ, Wang Q, Wyman DA, Li ZX, Zhao ZH and Yang YH** (2012) Late Carboniferous high $\epsilon_{\text{Nd}}(t)$ – $\epsilon_{\text{Hf}}(t)$ granitoids, enclaves and dikes in western Junggar, NW China: ridge-subduction-related magmatism and crustal growth. *Lithos* **140–141**, 86–102.
- Tiepolo M, Bottazzi P, Foley SF, Oberti R, Vannucci R, Zanetti A** (2001) Fractionation of Nb and Ta from Zr and Hf at mantle depths: the role of titanite, pargasite and kaersutite. *Journal of Petrology* **42**, 221–32.
- Tindle AG and Pearce JA** (1983) Assimilation and partial melting of continental crust: evidence from the mineralogy and geochemistry of autochthonous and xenoliths. *Lithos* **16**, 185–202.
- Vernon RH** (1984) Microgranitoid enclaves in granites; globules of hybrid magma quenched in a plutonic environment. *Nature* **309**, 438–9.
- Waight TE, Maas R and Nicholls IA** (2001) Geochemical investigations of microgranitoid enclaves in the S-type Cowra granodiorite, Lachlan Fold Belt, SE Australia. *Lithos* **56**, 165–86.
- Wan YS, Liu DY, Wilde SA, Cao JJ, Chen B, Dong CY, Song B and Du LL** (2010) Evolution of the Yunkai terrane, South China: evidence from SHRIMP zircon U–Pb dating, geochemistry and Nd isotope. *Journal of Asian Earth Science* **37**, 140–53.
- Wang YJ, Fan WM, Zhang GW and Zhang YH** (2013a) Phanerozoic tectonics of the South China Block: key observations and controversies. *Gondwana Research* **23**, 1273–305.
- Wang Q, Li XH, Jia XH, Wyman DA, Tang GJ, Li ZX, Ma L, Yang YH, Jiang ZQ and Gou GN** (2012) Late Early Cretaceous adakitic granitoids and associated magnesian and potassium-rich mafic enclaves and dikes in the Tunchang–Fengmu area, Hainan Province (South China): partial melting of lower crust and mantle, and magma hybridization. *Chemical Geology* **328**, 222–43.
- Wang LX, Ma CQ, Zhang C, Zhang JY and Marks MAW** (2014) Genesis of leucogranite by prolonged fractional crystallization: a case study of the Mufushan complex, South China. *Lithos* **206–207**, 147–63.
- Wang Q, Xu JF, Jian P, Bao ZW, Zhao ZH, Li CF, Xiong XL and Ma JL** (2006) Petrogenesis of adakitic porphyries in an extensional tectonic setting, Dexing, South China: implications for the genesis of porphyry copper mineralization. *Journal of Petrology* **47**, 119–44.
- Wang YJ, Zhang AM, Fan WM, Zhang YH and Zhang YZ** (2013b) Origin of paleosubduction-modified mantle for Silurian gabbro in the Cathaysia Block: geochronological and geochemical evidence. *Lithos* **160–161**, 37–54.
- Wang YJ, Zhang AM, Fan WM, Zhao GW, Zhang GW, Zhang YZ, Zhang FF and Li SZ** (2011) Kwangian crustal anatexis within the eastern South China Block: geochemical, zircon U–Pb geochronological and Hf isotopic fingerprints from the gneissoid granites of Wugong and Wuyi–Yunkai domains. *Lithos* **127**, 239–60.
- Wei GJ, Liang XR, Li XH and Liu Y** (2002) Precise measurement of Sr isotopic composition of liquid and solid base using (LP) MC-ICPMS. *Geochimica* **31**, 295–305 (in Chinese with English abstract).
- White AR, Chappell BW and Wyborn D** (1999) Application of the restite model to the Deddick Granodiorite and its enclaves—a reinterpretation of the observations and data of Maas et al. (1997). *Journal of Petrology* **40**, 413–21.
- Wiedenbeck M, Alle P, Corfu F, Griffin F, Meier M, Oberli F, Quadt AV, Roddick J and Spiegel W** (1995) Three natural zircon standards for U–Th–Pb, Lu–Hf, trace element and REE analyses. *Geostandards Newsletter* **19**, 1–23.
- Winter JD** (2009) *Principles of Igneous and Metamorphic Petrology, 2nd Ed.* Upper Saddle River, NJ: Prentice Hall.
- Wu FY, Jahn BM, Wilde SA, Lo CH and Sun DY** (2003) Highly fractionated I-type granites in NE China (I): geochronology and petrogenesis. *Lithos* **66**, 241–73.
- Wu FY, Sun DY, Jahn BM and Wilde SA** (2004) A Jurassic garnet-bearing granitic pluton from NE China showing tetrad REE patterns. *Journal of Asian Earth Science* **23**, 731–44.
- Wu FY, Yang YH, Xie LW, Yang JH and Xu P** (2006) Hf isotopic compositions of the standard zircons and baddeleyites used in U–Pb geochronology. *Chemical Geology* **234**, 105–26.
- Xu WL, Gao S, Wang QH, Wang DY, Liu YS** (2006) Mesozoic crustal thickening of the eastern North China craton: evidence from eclogite xenoliths and petrologic implications. *Geology* **34**, 721–4.
- Yang ZY, Wang Q, Zhang CF, Dan W, Zhang XZ, Qi Y, Xia XP and Zhao ZH** (2018) Rare earth element tetrads and negative Ce anomalies of the granite porphyries in southern Qiangtang Terrane, central Tibet: new insights into the genesis of highly evolved granites. *Lithos* **312–313**, 258–73.
- Yang JH, Wu FY, Wilde SA and Liu XM** (2007a) Petrogenesis of Late Triassic granitoids and their enclaves with implications for post-collisional lithospheric thinning of the Liaodong Peninsula, North China Craton. *Chemical Geology* **242**, 155–75.
- Yang JH, Wu FY, Wilde SA, Xie LW, Yang YH and Liu XM** (2007b) Tracing magma mixing in granite genesis: *in situ* U–Pb dating and Hf-isotope analysis of zircons. *Contributions to Mineralogy and Petrology* **153**, 177–90.
- Yao WH, Li ZX, Li WX, Wang XC, Li XH and Yang JH** (2012) Post-kinematic lithospheric delamination of the Wuyi–Yunkai orogen in South China: evidence from ca. 435 Ma high-Mg basalts. *Lithos* **154**, 115–29.
- Yao JL, Shu LS, Santosh M and Zhao GC** (2014) Neoproterozoic arc-related mafic–ultramafic rocks and syn-collision granite from the western segment of the Jiangnan Orogen, South China: constraints on the Neoproterozoic assembly of the Yangtze and Cathaysia Blocks. *Precambrian Research* **243**, 39–62.
- Yu JH, O'Reilly SY, Wang LJ, Griffin WL, Zhou MF, Zhang M and Shu LS** (2010) Components and episodic growth of Precambrian crust in the Cathaysia Block, South China: evidence from U–Pb ages and Hf isotopes of zircons in Neoproterozoic sediments. *Precambrian Research* **181**, 97–114.
- Yu JH, Wang LJ, Griffin WL, O'Reilly SY, Zhang M, Li CZ and Shu LS** (2009) A Paleoproterozoic orogeny recorded in a long-lived cratonic remnant (Wuyishan terrane), eastern Cathaysia Block, China. *Precambrian Research* **174**, 347–63.
- Zeng LS, Asimow PD and Saleeby JB** (2005a) Coupling of anatectic reactions and dissolution of accessory phases and the Sr and Nd isotope systematics of anatectic melts from a metasedimentary source. *Geochimica et Cosmochimica Acta* **69**, 3671–82.
- Zeng LS, Saleeby JB and Asimow PD** (2005b) Nd isotope disequilibrium during crustal anatexis: a record from the Goat Ranch migmatite complex, southern Sierra Nevada batholith, California. *Geology* **33**, 53–6.
- Zhang ZJ and Wang YH** (2007) Crustal structure and contact relationship revealed from deep seismic sounding data in South China. *Physics of the Earth and Planetary Interiors* **165**, 114–26.
- Zhang JJ, Wang T, Castro A, Zhang L, Shi XJ, Tong Y, Zhang ZC, Guo L, Yang QD and Iaccheri LM** (2016) Multiple mixing and hybridization from magma source to final emplacement in the Permian Yamatu pluton, the Northern Alxa Block, China. *Journal of Petrology* **57**, 933–80.
- Zhang FF, Wang YJ, Zhang AM, Fan WM, Zhang YZ and Zi JW** (2012) Geochronological and geochemical constraints on the petrogenesis of Middle Paleozoic (Kwangian) massive granites in the eastern South China Block. *Lithos* **150**, 188–208.

- Zhang SB, Zheng YF, Wu YB, Zhao ZF, Gao S and Wu FY** (2006) Zircon U–Pb age and Hf–O isotope evidence for Paleoproterozoic metamorphic event in South China. *Precambrian Research* **151**, 265–88.
- Zhong YF, Ma CQ, Liu L, Zhao JH, Zheng JP, Nong JN and Zhang ZJ** (2014) Ordovician appinites in the Wugongshan Domain of the Cathaysia Block, South China: geochronological and geochemical evidence for intrusion into a local extensional zone within an intracontinental regime. *Lithos* **198–199**, 202–16.
- Zhong YF, Ma CQ, Zhang C, Wang SM, She ZB, Liu L and Xu HB** (2013) Zircon U–Pb age, Hf isotopic compositions and geochemistry of the Silurian Fengdingshan I-type granite pluton and Taoyuan mafic–felsic complex at the southeastern margin of the Yangtze Block. *Journal of Asian Earth Science* **74**, 11–24.